Check for updates

Received: 20 March 2023 | Revised: 10 January 2024 | Accepted: 15 January 2024

DOI: 10.1002/nag.3695

RESEARCH ARTICLE

WILEY

A new cube movement test for verification of simulations of contact processes of blocks of different size in geological hazards

Xinquan Wang[1,2,3] | Chun Feng[2,3] | Olaf Lahayne[1] | Yiming Zhang[4] | Herbert A. Mang[1,5] | Bernhard L. A. Pichler[1]

[1]Institute for Mechanics of Materials and Structures, TU Wien (Vienna University of Technology), Vienna, Austria

[2]Institute of Mechanics, Chinese Academy of Sciences, Beijing, China

[3]School of Engineering Science, University of Chinese Academy of Sciences, Beijing, China

[4]School of Civil and Transportation Engineering, Hebei University of Technology, Tianjin, China

[5]College of Civil Engineering, Tongji University, Shanghai, China

Correspondence
Bernhard L. A. Pichler, Institute for Mechanics of Materials and Structures, TU Wien (Vienna University of Technology), Karlsplatz 13/202, 1040 Vienna, Austria.
Email: Bernhard.Pichler@tuwien.ac.at

Funding information
China Scholarship Council; National Key Research and Development Program of China, Grant/Award Number: No. 2018YFC1505504

Abstract

In many geological hazards, such as landslides, a large number of irregular blocks start moving. Their interaction on the way down renders prediction of disaster scopes difficult. To study this process and to provide a novel method for validation and calibration of numerical tools for its simulation, a cube movement test is designed. The goal of this research is to obtain patterns of movement of cubes, starting from different initial stacking arrangements. Cubes of four sizes are inserted into a hollow cylinder. Their distribution after lifting the cylinder is determined. Three categories of tests refer to three different strategies of filling the cubes into the cylinder. In order to simulate cube movement tests, a numerical tool is developed in the framework of the continuum–discontinuum element method (CDEM). The contact between the individual cubes is modeled by the contact-pairs-based algorithm. Both the contact state and type are detected by determining the half-space relation between contact pairs. The final positions of the cubes are strongly related to their initial arrangement. The latter is different in every test, even if the same strategy is used to fill the cubes into the cylinder. It is found that at least 20 experiments/simulations are required to obtain statistically representative results. The new test provides valuable data for validation of numerical tools used for the simulation of mass movement processes. The proposed numerical method captures the complicated movements of blocks.

KEYWORDS

contact detection, continuum–discontinuum element method, irregular polyhedra, mass movement

This is an open access article under the terms of the Creative Commons Attribution-NonCommercial License, which permits use, distribution and reproduction in any medium, provided the original work is properly cited and is not used for commercial purposes.
© 2024 The Authors. *International Journal for Numerical and Analytical Methods in Geomechanics* published by John Wiley & Sons Ltd.

1 INTRODUCTION

In geological hazards, such as rocky landslides and debris flows, a large number of irregular rock boulders is involved in their motion, including contact and collision.[1,2] When the rock body fractures and moves along the damaged surface, encountering large displacements, the discontinuous characteristics of the rock body need to be considered. Several simulation methods use a particle- or block-based approach to develop geological models, paying attention to the discontinuous characteristics in geological problems. These simulation methods include the discrete element method (DEM),[3] discontinuous deformation analysis (DDA),[4,5] the numerical manifold method (NMM),[6,7] the material point method (MPM),[8,9] smoothed particle hydrodynamics (SPH),[10,11] and the finite-discrete element method (FDEM).[12] Another method is the continuum–discontinuum element method (CDEM). It is a hybrid method that can simulate the whole process from a continuous to a discontinuous geological body.[13,14] The CDEM was successfully applied to the analysis of a variety of geotechnical engineering problems, such as coal caving mining,[15] propagation of hydrofracturing cracks,[16,17] rock blasting,[18,19] crack propagation of brittle materials,[20,21] deformation of tunnels,[22] and landslides.[23,24] The success of modern simulation models for granular matter requires realistic and efficient consideration of frequently complex particle shapes of geological materials, see Zhao et al.[25] for a comprehensive appraisal of state-of-the-art computational models for granular particles of either naturally occurring shapes or engineered geometries.

The collision of blocks results in contact forces. The subsequent movement of the blocks is influenced by their contact. Modeling of contact exerts an influence on the results of the simulation.[26,27] Because of the need to simulate the movement characteristics of discontinuous rock mass, as with all other simulation methods that consider discrete properties, the CDEM requires robust contact-detection algorithms for describing the contact state between the blocks.[28,29] Contact detection methods remain a major challenge in discrete element calculations. Contact between the blocks needs to be continuously identified and updated throughout the computation. The contact-detection algorithm must be accurate and efficient.

For irregular elements, such as irregularly shaped particles[23,30] and polygonal and polyhedral blocks, contact methods are complex. The common plane method[31] is one of the generally used search methods. The contact relations are determined by finding the common plane between the blocks. The fast common plane method,[32] the shortest link method,[33] and other noniterative common plane methods[34,35] are developed, based on the common plane theory. The entrance-block method[36] is another contact detection theory. It converts the contact relation between two blocks into a contact relationship between a point and an entrance block. Based on this contact theory, cover-based contact detection methods[37–39] have been developed. Potential-based penalty function methods are established to calculate the contact forces.[40–42] Because of the irregularity of polyhedra, algorithms for complete contact search and efficient contact identification are difficult to develop. The establishment of an effective contact detection theory is a very difficult task.

After contact is detected, the corresponding contact force is to be calculated. There are two kinds of related methods. One of them allows contact bodies to overlap, and the contact force is calculated based on the penetration volume. Such methods are also called "soft-dem" approaches.[43] Examples of this strategy are the penalty method proposed by Cundall[3] and the potential-based penalty function methods.[40–42] These methods use an explicit approach. The other kind is based on the contact dynamics method.[44–46] It ensures that there is no overlap in the contact area. Such methods are also called "rigid-dem" approaches.[47] The contact forces are applied as constraints at the contact points. Examples of this procedure are the Lagrangian multiplier method,[48] and the augmented Lagrange formulation.[49] Both of them use an implicit approach.

Geological bodies are cut by different joints to form polyhedra. Many numerical benchmark tests use blocks of the same size to show the accuracy of the underlying algorithms. This enables checking the consistency between numerical results and experimental or analytical results. However, in real situations, the sizes of the blocks are different. This results in different characteristics of the movement of the blocks.[50,51] In this study, experiments with cubes of different size are carried out. The steps of the experiment refer to the hollow-cylinder test, which has been widely used to test the properties of granular materials.[52–54] The regularities of the motion of cubes with four different sizes, starting from three different arrangements, are studied. The simulations are performed, considering the same situation as in the experiments. The contact status is detected by the half-space-based contact-detection algorithm.[29] Herein, the subsequent identification of the contact type is improved by taking into account the location and the number of contact pairs that satisfy the half-space inclusion relation in the last step. This has the advantage that missed or inaccurate contact detection is avoided. The contact forces are calculated based on the penalty function method.[3,55]

The paper is organized as follows: The cube movement tests are documented in Section 2, including tests of material properties, experimental settings, and the results of tests for three types of initial cube arrangement. A brief review of

10969853, 2024, 6, Downloaded from https://onlinelibrary.wiley.com/doi/10.1002/nag.3695 by Readcube (Labtiva Inc.), Wiley Online Library on [07/11/2024]. See the Terms and Conditions (https://onlinelibrary.wiley.com/terms-and-conditions) on Wiley Online Library for rules of use; OA articles are governed by the applicable Creative Commons License

10969853, 2024, 6, Downloaded from https://onlinelibrary.wiley.com/doi/10.1002/nag.3695 by Readcube (Labtiva Inc.), Wiley Online Library on [07/11/2024]. See the Terms and Conditions (https://onlinelibrary.wiley.com/terms-and-conditions) on Wiley Online Library for rules of use; OA articles are governed by the applicable Creative Commons License

TABLE 1 Side lengths of the PVC cubes and their numbers.

Side length of cubes [mm]	20	16	12	8	Total
Number of cubes [–]	4	8	20	68	100
Total volume [mm^3]	32,000	32,768	34,560	34,816	134,144

TABLE 2 Properties of the PVC, out of which the cubes are made.

Physical property	Value
Mass density ρ	$1.406 \pm 0.006\,\mathrm{kg/m^3}$
Longitudinal wave speed v_l	$2.386 \pm 0.011\,\mathrm{km/s}$
Transversal wave speed v_t	$1.025 \pm 0.008\,\mathrm{km/s}$
Modulus of elasticity E	$4.085 \pm 0.066\,\mathrm{GPa}$
Poisson's ratio ν	$0.387 \pm 0.002\mathrm{GPa}$

the formulation of the CDEM and the contact-detection algorithms for polyhedral blocks is presented in Section 3. The simulation process and the results are also described in Section 3. A comparison of experimental and simulation results is presented in Section 4. After a discussion in Section 5, the main conclusions are drawn in Section 6.

2 | PULL-UP OF A HOLLOW CYLINDER FILLED WITH PVC CUBES OF DIFFERENT SIZE

A laboratory test, mimicking a geological mass movement problem, is developed. After inserting cubes made of polyvinyl chloride (PVC) into a hollow polymethyl methacrylate (PMMA) cylinder, the latter is pulled upwards, the cubes run out of it, and they come to rest in a specific distribution pattern which is documented. The approach is conceptually similar to slump tests used for determination of the consistency of freshly mixed concrete,[56,57] angle of repose tests used in powder technology,[52] and mass movement tests performed with objects of the same size and shapes.[58]

The use of cubes of *four different sizes* and the implementation of *three different strategies* to fill them into the hollow PMMA cylinder are two new features of the performed tests. One hundred cubes are used for every test: four cubes with a side length amounting to 20 mm, eight cubes with 16 mm, 20 cubes with 12 mm, and 68 cubes with 8 mm, see Table 1. The cubes are cut from a large piece of PVC material. The edges remained as sharp as they were, that is, no postprocessing such as smoothening was carried out. The inner diameter of the cylinder is chosen as three times the side length of the largest cube, that is, 60 mm. The outer radius is 70 mm. A cylindrical coordinate system is introduced. Its origin is located at the center of the circle at the bottom of the PMMA cylinder. The z-axis coincides with the axis of the PMMA cylinder and runs upwards. Three different strategies are used to fill the cubes into the cylinder.

1. "Negative size-gradient arrangement": At first, the 20-mm cubes are inserted into the cylinder, followed by the 16-, 12-, and 8-mm cubes.
2. "Positive size-gradient arrangement": At first, the 8-mm cubes are inserted into the cylinder, followed by the 12-, 16-, and 20-mm cubes.
3. "Random arrangement": All cubes are mixed in a bowl and inserted into the cylinder in a disordered fashion.

The tests are performed on a surface made of polyethylene terephthalate (PET). Concentric circles are printed on this surface, see Figure 1. The radial distance between neighboring circles amounts to 1 cm. The testing room is conditioned to 20°C.

2.1 | Production of PVC cubes and ultrasonic characterization of their elastic stiffness

The cubes were produced from one block of PVC using a three-axis CLC milling machine of type Kunzmann WF 7/3-320. It provides a nominal fabrication accuracy of 1 µm. The mass density ρ of the PVC material was quantified by dividing the mass of individual cubes by their volume, see Table 2.

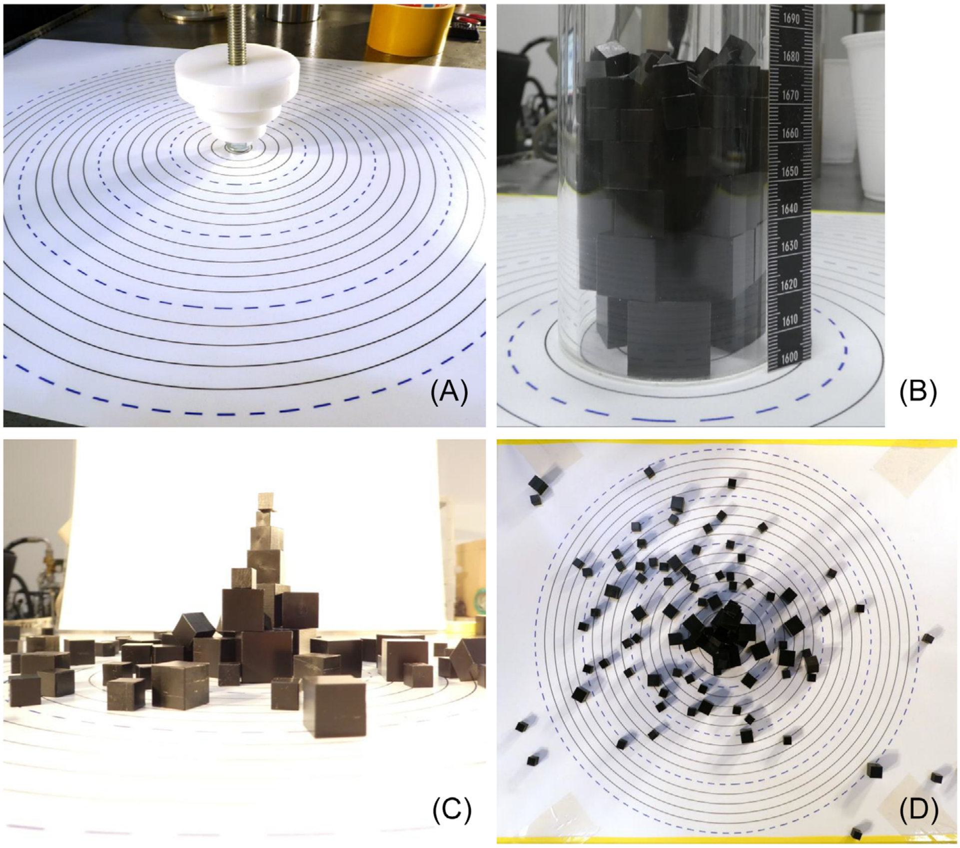

FIGURE 1 Characteristic stages of the experiments: (A) check of the alignment of the axis of the lifting system with the centers of the circles printed onto the PET surface, (B) initial arrangement of PVC cubes after their insertion into the hollow PMMA cylinder, (C) side view of the final position of the cubes, and (D) corresponding top view after removal of cubes which have ended up on other cubes.

As for characterization of the elastic stiffness of the used PVC, loading–unloading tests would activate viscoelastic material behavior, raising the need to evaluate such tests by means of the linear theory of viscoelasticity.[59] As a remedy, ultrasonic pulse velocity measurements are performed and evaluated by means of the theory of elastic wave propagation through isotropic media.[60] Corresponding expressions for the modulus of elasticity, E, and Poisson's ratio, ν, read as

$$E = \frac{\rho\, v_t^2\,(3v_l^2 - 4v_t^2)}{v_l^2 - v_t^2}\,, \tag{1}$$

$$\nu = \frac{v_l^2 - 2v_t^2}{2(v_l^2 - v_t^2)}\,, \tag{2}$$

where v_l and v_t denote longitudinal and transversal wave speeds. In order to quantify them, one cube of each size was tested. Four individual tests are performed in all three possible directions, using both longitudinal and transversal waves with a central frequency of 5 MHz. This results in a database of 48 pairs of longitudinal and transversal wave velocities. They are virtually independent of the cube size and the measurement direction, see Table 2 for mean values and standard deviations. Evaluation of Equations (1) and (2) based on values of ρ, v_l, and v_t from Table 2 yields values of E and ν also listed in Table 2. The values of E are, for example, typically located in an interval ranging from 2.5 to 5.5 GPa.[61]

2.2 | Determination of friction coefficients

The friction coefficients, μ, are determined by means of sliding experiments. A PVC cube is put on a PVC plate made from the same material. The inclination of the plate is increased slowly until the cube starts sliding. The corresponding value of the angle of inclination φ is measured. It allows for quantification of the coefficient of friction as $\mu = \tan\varphi$.

10969853, 2024, 6, Downloaded from https://onlinelibrary.wiley.com/doi/10.1002/nag.3695 by Readcube (Labtiva Inc.), Wiley Online Library on [07/11/2024]. See the Terms and Conditions (https://onlinelibrary.wiley.com/terms-and-conditions) on Wiley Online Library for rules of use; OA articles are governed by the applicable Creative Commons License

10969853, 2024, 6, Downloaded from https://onlinelibrary.wiley.com/doi/10.1002/nag.3695 by Readcube (Labtiva Inc.), Wiley Online Library on [07/11/2024]. See the Terms and Conditions (https://onlinelibrary.wiley.com/terms-and-conditions) on Wiley Online Library for rules of use; OA articles are governed by the applicable Creative Commons License

TABLE 3 Values of coefficients of friction between PVC cubes and a PVC plate, the PET surface, and the PMMA cylinder, respectively.

Side length of cubes [mm]	20	16	12	8
PVC cubes on a PVC plate	0.262	0.271	0.314	0.443
PVC cubes on the PET surface	0.305	0.316	0.358	0.444
PVC cubes in the hollow PMMA cylinder	0.274	0.287	0.303	0.356

TABLE 4 Coefficients of restitution according to Equation (3) as a function of the size of the PVC cubes.

Side length of cubes [mm]	20	16	12	8
H_1 [cm]	5.6	7.7	5.3	6.8
R	0.43	0.51	0.42	0.48

Performing such tests with cubes of all four sizes yields the values of the friction coefficients listed in Table 3. They are inside the range of PVC-on-PVC friction coefficients reported in the literature.[61] The same type of experiment is performed for quantification of values of coefficients of friction between the PVC cubes and the PET surface, see Table 3. As regards friction between the PVC cubes and the hollow PMMA cylinder, one cube is put into the cylinder such that contact prevails along two edges of the cube. The inclination of the cylinder is increased until the cube starts sliding along the contact edges, see Table 3 for values of friction coefficients.

2.3 | Determination of coefficients of restitution

The coefficient of restitution R is determined by means of drop tests.[62] Individual cubes of all sizes are dropped, one after the other, from a height H_0 amounting to 30 cm. This is done in a way that the cubes impact with a side face, rather than with an edge or a corner, onto the PET surface. The impact of each cube and the rebound from the PET surface are recorded with a camera. The height of rebound, H_1, of each cube is measured by means of a ruler, which is positioned vertically in the immediate vicinity of the falling cube, see Table 4 for results. The coefficient of restitution, R, is quantified as

$$R = \sqrt{\frac{H_1}{H_0}}, \tag{3}$$

see Table 4 for values of R obtained for the four different sizes of the cubes.

2.4 | Performing and documenting cube movement tests

The cylinder containing the cubes is lifted, using a servohydraulic testing machine of type Walter und Bai/DLFV-250/DZ-10-D, see Figure 2. The maximum strokes of both hydraulic cylinders of this machine are too small for lifting the hollow PMMA cylinder high enough to ensure a complete run-out of the cubes. As a remedy, the upper end of the PMMA cylinder is fixed to the crosshead of the testing machine. The cross head is hydraulically moved upwards at a speed of 28 mm/s until all cubes have run out of the cylinder.

Once all cubes have reached a stable final position, see Figure 1C, the obtained arrangement is documented by counting the number of cubes ending up in 19 specific regions. The first region is equal to the area of the PET surface, which is initially inside the PMMA cylinder. This circular region has a radius of 3 cm and is referred to as "Position 3 cm." The next 17 regions have annular shapes. The radial width of all annuli is equal to 1 cm. The innermost annular region has an inner radius of 3 cm and an outer radius of 4 cm. It is referred to as "Position 4 cm." The outermost annular region has an inner radius of 19 cm and an outer radius of 20 cm. It is referred to as "Position 20 cm." The last region refers to the area of the PET surface, with a radial distance from the axis of the experiment larger than 20 cm. For the sake of simplicity, it is referred to as "Position 21 cm."

Each cube is assigned to one of these 19 regions. To this end, its center of gravity is projected vertically downwards onto the PET surface. The obtained point is inside one specific region. It is assigned to the cube. This assignment is performed by means of the following two-step procedure. Step 1 refers to cubes ending up on top of other cubes, see Figure 1C. These cubes are visually assigned to the respective regions and then manually removed without changing the positions of the

FIGURE 2 Servohydraulic testing machine used for the cube movement experiments.

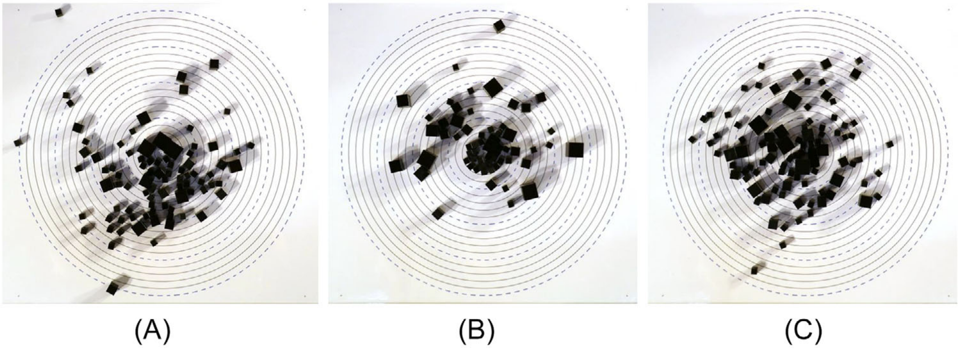

FIGURE 3 Photos showing distribution patterns resulting from tests which for three different initial arrangements: (A) negative size-gradient, (B) positive size-gradient, and (C) random arrangement.

other cubes. Step 2 refers to cubes ending up directly on the PET surface. A photo of these cubes, taken from the top, is shown in Figure 1D. Post-processing by means of image analysis software allows for automatically assigning the cubes to the different regions.

2.5 | Results from cube movement tests

Each cube movement test delivers a unique result. Different initial arrangements of the cubes provide different results, see Figure 3, containing photos of the distribution patterns of the cubes after the start of tests for the three different types of initial arrangements. Notably, these photos were taken after the classification and removal of cubes ending up on top of other cubes. Corresponding test results in terms of numbers of cubes, ending up in the different regions, are illustrated in Figure 4. The distribution of the 8-mm cubes may look quite similar when comparing results obtained with the "negative

10969853, 2024, 6, Downloaded from https://onlinelibrary.wiley.com/doi/10.1002/nag.3695 by Readcube (Labtiva Inc.), Wiley Online Library on [07/11/2024]. See the Terms and Conditions (https://onlinelibrary.wiley.com/terms-and-conditions) on Wiley Online Library for rules of use; OA articles are governed by the applicable Creative Commons License

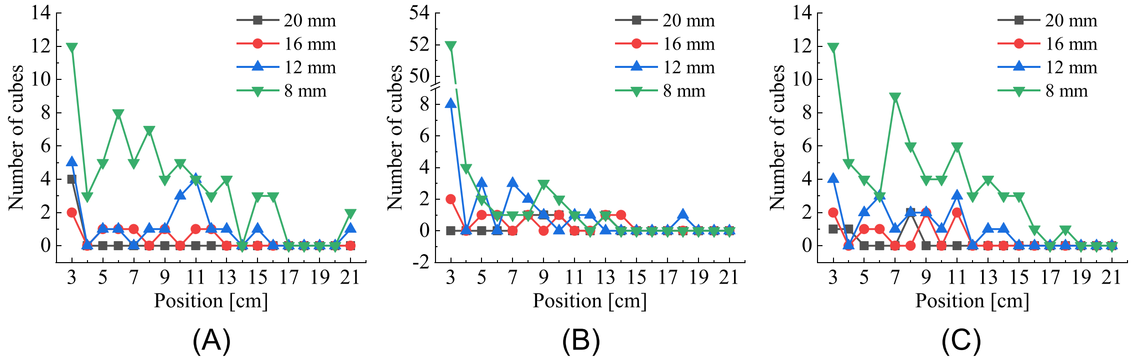

FIGURE 4 Number of cubes ending up in different regions, resulting from tests which for three different initial arrangements: (A) negative size-gradient, (B) positive size-gradient, and (C) random arrangement.

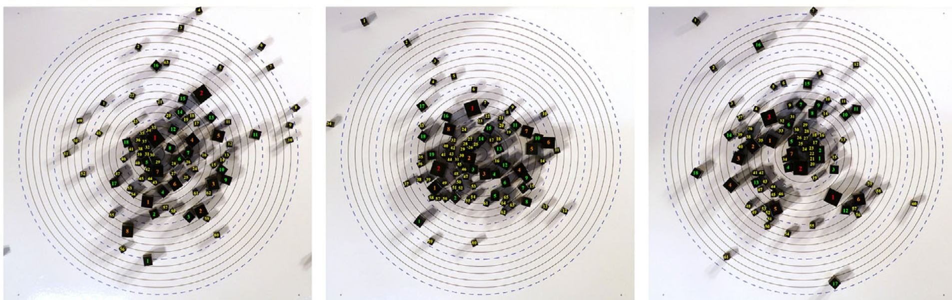

FIGURE 5 Photos showing distribution patterns obtained from three different tests, starting from a "random arrangement" of the cubes.

size-gradient arrangement" and the "random arrangement," see Figure 4A,C. However, many more 8-mm cubes stay very close to the center when starting the test from the "positive size-gradient arrangement," see Figure 4B, noting that the ordinate interval from 9 to 49 is cut out.

There is also a noticeable dispersion of the experimental results when comparing distribution patterns obtained from *different* tests for *the same* type of initial arrangements, see for example Figure 5 for results referring to an initial "random arrangement." These results indicate that it is necessary to repeat the tests several times, in order to get statistically representative results. One hundred and twenty cube movement tests were performed, that is, 40 tests for each one of the three strategies used to fill the cubes into the hollow cylinder, see Tables A.2, B.2, and C.2. For the tests that started from "random arrangements" of the cubes, see Table C.2, a convergence analysis was carried out for the sake of assessing whether or not enough tests were performed in order to obtain statistically representative results. The convergence analysis started with results from the first 10 tests. The mean values and the standard deviations of the number of cubes of a specific size, ending up in specific regions, were computed and illustrated, see the black graphs in Figure 6. This is repeated based on the results obtained from the first 20 tests and from all 40 tests, respectively, see the red and blue graphs in Figure 6. The mean values from the first 20 tests are quite similar to the ones resulting from all 40 tests. Thus, 20 tests appear to be enough in order to obtain statistically representative results.

3 | SIMULATION METHOD

3.1 | Formulation of the continuum–discontinuum element method

3.1.1 | Governing equations

The Lagrangian equations are given as

$$\frac{\mathrm{d}}{\mathrm{d}t}\frac{\partial L}{\partial \dot{u}_i} - \frac{\partial L}{\partial u_i} = Q_i\,, \tag{4}$$

10969853, 2024, 6, Downloaded from https://onlinelibrary.wiley.com/doi/10.1002/nag.3695 by Readcube (Labtiva Inc.), Wiley Online Library on [07/11/2024]. See the Terms and Conditions (https://onlinelibrary.wiley.com/terms-and-conditions) on Wiley Online Library for rules of use; OA articles are governed by the applicable Creative Commons License

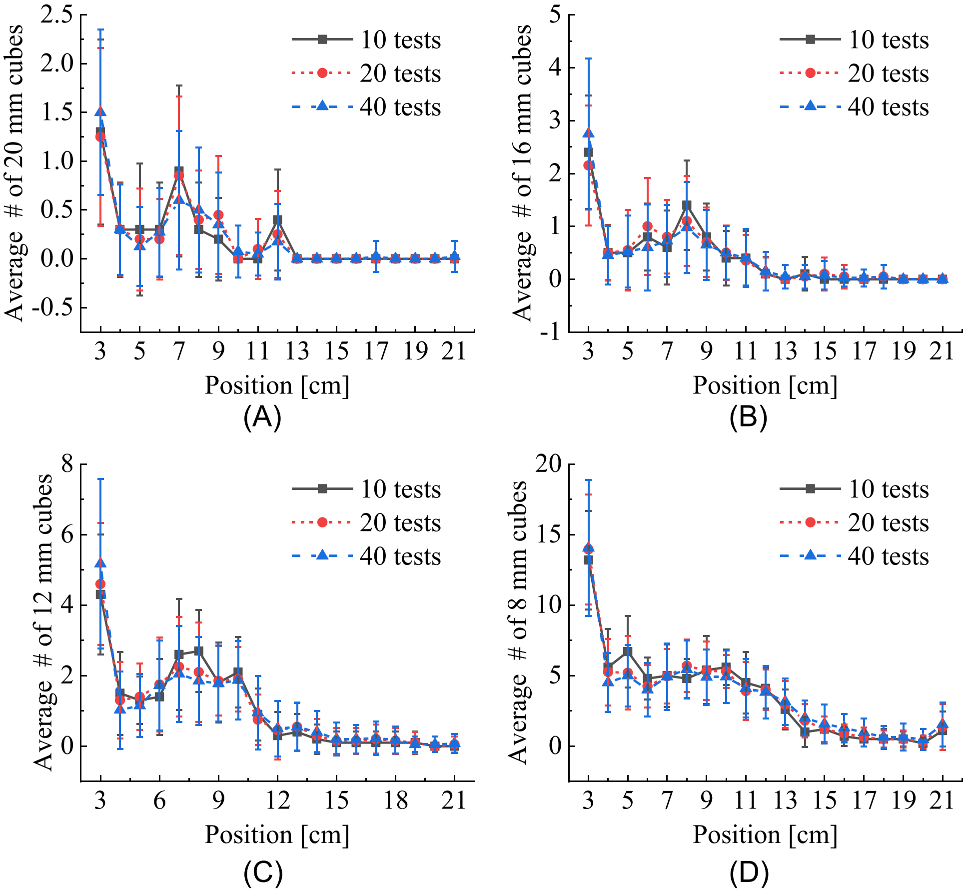

FIGURE 6 Convergence analysis of results obtained from cube movement tests for initial "random arrangements" of cubes, see Table C.2: mean values and standard deviations of the number of cubes ending up in specific regions, computed on the basis of the first 10, the first 20, and all 40 test results: (A) 20-mm cubes, (B) 16 mm cubes, (C) 12-mm cubes, and (D) 8-mm cubes.

where t stands for the time, L denotes the Lagrangian, u_i is a component of the displacement of node i of the element considered, $\dot{u}_i$ is the derivative of u_i with respect to time, that is, the corresponding velocity component of node i, and Q_i is a nonconservative force component at this node.

The governing state equations for an element are given as

$$\boldsymbol{M}\ddot{\boldsymbol{u}} + \boldsymbol{C}\dot{\boldsymbol{u}} + \boldsymbol{K}\boldsymbol{u} = \boldsymbol{F}\,, \tag{5}$$

where $\boldsymbol{M}$, $\boldsymbol{C}$, and $\boldsymbol{K}$ denote the element mass, damping, and stiffness matrix, respectively. $\boldsymbol{F}$ denotes the vector of external node forces. $\boldsymbol{u}$, $\dot{\boldsymbol{u}}$, and $\ddot{\boldsymbol{u}}$ stand for the displacement, velocity, and the acceleration vector, respectively.

3.1.2 | Explicit approach of the solution

The governing equations of the CDEM are solved by the dynamic relaxation method, which is an explicit method. The mass is concentrated at the nodes of the discrete elements, and the relationships between the nodes are defined in terms of the stiffness of the element. Only the stiffness matrices of the elements need to be calculated. Because the displacement at the current time step only depends on the velocity and the displacement of the previous time step, an iterative calculation of the global stiffness matrix, that is, the one of the whole block, is avoided.

The solution process can be divided into three steps: step 1 extends over the elements; it involves the calculation of the deformations and of the damping forces for each element, step 2 stretches over the interfaces; it involves the calculation of the contact conditions and the contact forces for each contact interface, step 3 extends over the nodes; it consists of the calculation of the external forces, accelerations, velocities, and displacements for each node.

10969853, 2024, 6, Downloaded from https://onlinelibrary.wiley.com/doi/10.1002/nag.3695 by Readcube (Labtiva Inc.), Wiley Online Library on [07/11/2024]. See the Terms and Conditions (https://onlinelibrary.wiley.com/terms-and-conditions) on Wiley Online Library for rules of use; OA articles are governed by the applicable Creative Commons License

The forward Euler difference method is used. To ensure numerical stability, a small time step Δt is required. The critical time step can be estimated by dividing the velocity of sound through the elements by the minimum size of the elements.[63] Δt should be smaller than the critical time step. The differential equations for the velocity and the displacement are given by

$$\begin{aligned} \dot{u}(t+\Delta t) &= \dot{u}(t) + \ddot{u}(t)\,\Delta t\,, \\ u(t+\Delta t) &= u(t) + \dot{u}(t)\,\Delta t\,. \end{aligned} \tag{6}$$

During the calculation process, the deviation of the results from an equilibrium state of the system is characterized by the imbalance ratio. Viscous damping is adopted to absorb part of the kinetic energy of the system and to make dynamic relaxation computationally more efficient. In the CDEM, the Rayleigh damping is adopted, the damping matrix is given as[64]

$$\boldsymbol{C} = \alpha_M \boldsymbol{M} + \alpha_K \boldsymbol{K}\,, \tag{7}$$

In the present study, only the stiffness damping is employed ($\alpha_M = 0$). The stiffness damping is applied on the element, which is treated as equivalent to the damping applied on the contact spring. For a linear single degree of freedom system, α_K is given as

$$\alpha_K = \frac{2\zeta}{\sqrt{K_n/m}}\,, \tag{8}$$

where ζ denotes the critical damping ratio, K_n stands for the normal contact stiffness, and m denotes the mass. According to the linear spring-dashpot contact model,[65,66] the critical damping ratio ζ is expressed as

$$\zeta = -\frac{\ln R}{\sqrt{\ln^2 R + \pi^2}}\,, \tag{9}$$

where R is the coefficient of restitution, see Table 4.

3.2 | Contact-pairs-based contact algorithm

The simulation of the movement of the cubes involves many contacts between them. A contact-pairs-based contact-detection algorithm[29] for an irregular polyhedron is used in this study. Its geometry is described in terms of half-spaces. The polyhedron is assumed to be the intersection of multiple half-spaces. The contact-detection algorithm consists of two stages: the stage of contact-status detection and the one of contact-type identification. In the first stage, the contact status is detected by the half-space inclusion relations of the contact pairs. After detection of a contact, the next step is contact-type identification. In the original method,[29] the contact type was identified by the location of the contact point. In the present study, this approach is improved. The contact type is determined by the location and the number of contact pairs that satisfy the half-space inclusion relation in the last step. The contact detection algorithm is implemented in the framework of the CDEM.

3.2.1 | Contact-status detection

A three-dimensional half-space (see Figure 7) can be defined as

$$(\boldsymbol{p} - \boldsymbol{a}) \cdot \boldsymbol{n} \geq 0\,, \tag{10}$$

where $\boldsymbol{p}$ denotes the space vector of an arbitrary point in the half-space, $\boldsymbol{a}$ is a space vector directed to a point on the boundary of the half-space, and $\boldsymbol{n}$ stands for the vector, normal to this boundary. The half-space is located on the side of the face to which $\boldsymbol{n}$ is pointing.

10969853, 2024, 6, Downloaded from https://onlinelibrary.wiley.com/doi/10.1002/nag.3695 by Readcube (Labtiva Inc.), Wiley Online Library on [07/11/2024]. See the Terms and Conditions (https://onlinelibrary.wiley.com/terms-and-conditions) on Wiley Online Library for rules of use; OA articles are governed by the applicable Creative Commons License

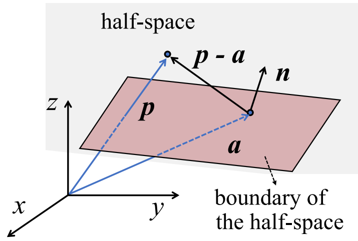

FIGURE 7 Definition of a half-space.

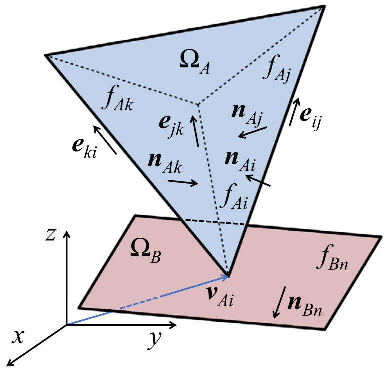

FIGURE 8 V–F potential contact pair.

In this case, the face i of a polyhedron is denoted as f_i. The plane in which f_i is located is the boundary of a half-space, defined as

$$(\boldsymbol{p}-\boldsymbol{a}_i)\cdot\boldsymbol{n}_i = 0\,, \qquad i = 1,\, 2,\, \ldots,\, n\,, \tag{11}$$

where $\boldsymbol{a}_i$ and $\boldsymbol{n}_i$ are the space vector and the "inner normal vector" of face i of a polyhedron, respectively. The "inner normal vector" points to the interior of the polyhedron.

An edge can be defined as the line of intersection of two faces. A vertex can be defined as the intersection point of three or more faces. A convex polyhedron Ω_A with n faces can be defined as the intersection of n half-spaces,

$$(\boldsymbol{p}-\boldsymbol{a}_i)\cdot\boldsymbol{n}_i \geq 0\,, \qquad i = 1,\, 2,\, \ldots,\, n\,. \tag{12}$$

At the contact-status detection stage, all six contact types are summarized to vertex–face (V–F) contacts and edge–edge (E–E) contacts. At this stage, the V–F potential contact pair and the E–E potential contact pair are identified. By examining the relation between the vertex and the face in the V–F potential contact pair and the one between edge and edge in the E–E potential contact pair, the contact status between two polyhedral blocks can be detected.[29]

For a V–F potential contact pair, consider a vertex formed by the intersection of three faces, see Figure 8. $\boldsymbol{v}_{Ai}$ defines the space vector of a vertex of polyhedron Ω_A. f_{Ai}, f_{Aj}, and f_{Ak} denote the faces, in counterclockwise order, the intersections of which result in this vertex. $\boldsymbol{n}_{Ai}$, $\boldsymbol{n}_{Aj}$, and $\boldsymbol{n}_{Ak}$ are the inner normal vectors of these faces. In case of vertices formed by more than three faces, the situation is analogous. f_{Bn} stands for a face of polyhedron Ω_B, while $\boldsymbol{n}_{Bn}$ denotes the inner normal vector of this face.

The vertex vectors $\boldsymbol{e}_{ij}$, $\boldsymbol{e}_{jk}$, $\boldsymbol{e}_{ki}$ are defined as

$$\begin{aligned}\boldsymbol{e}_{ij} &= \boldsymbol{n}_{Ai}\times\boldsymbol{n}_{Aj}\,,\\ \boldsymbol{e}_{jk} &= \boldsymbol{n}_{Aj}\times\boldsymbol{n}_{Ak}\,,\\ \boldsymbol{e}_{ki} &= \boldsymbol{n}_{Ak}\times\boldsymbol{n}_{Ai}\,.\end{aligned} \tag{13}$$

10969853, 2024, 6, Downloaded from https://onlinelibrary.wiley.com/doi/10.1002/nag.3695 by Readcube (Labtiva Inc.), Wiley Online Library on [07/11/2024]. See the Terms and Conditions (https://onlinelibrary.wiley.com/terms-and-conditions) on Wiley Online Library for rules of use; OA articles are governed by the applicable Creative Commons License

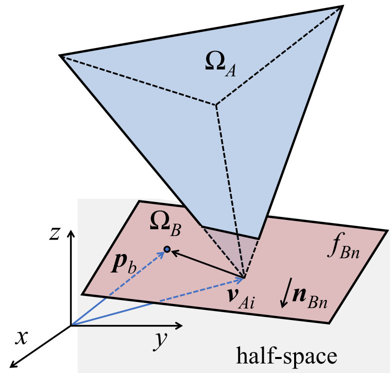

FIGURE 9 Half-space inclusion relation of a V–F potential contact pair.

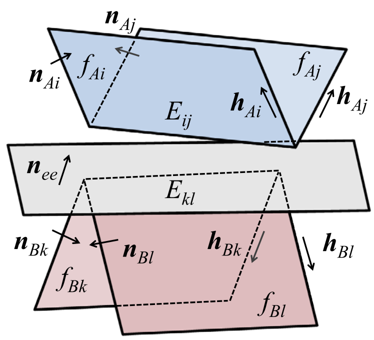

FIGURE 10 E–E potential contact pair.

Because the faces are labeled in counterclockwise order and the angles between two adjacent faces are less than 180°, the vectors point off from the vertex v_{Ai}. A V–F potential contact pair (see Figure 8) is defined as

$$\begin{aligned} \boldsymbol{e}_{ij} \cdot \boldsymbol{n}_{Bn} &\leq 0\,, \\ \boldsymbol{e}_{jk} \cdot \boldsymbol{n}_{Bn} &\leq 0\,, \\ \boldsymbol{e}_{ki} \cdot \boldsymbol{n}_{Bn} &\leq 0\,. \end{aligned} \tag{14}$$

Given a point on face f_{Bn}, defined by its space vector $\boldsymbol{p}_b$, see Figure 9. If the direction vector $(\boldsymbol{p}_b - \boldsymbol{v}_{Ai})$ satisfies the condition

$$(\boldsymbol{p}_b - \boldsymbol{v}_{Ai}) \cdot \boldsymbol{n}_{Bn} \leq 0\,, \tag{15}$$

the vertex defined by $\boldsymbol{v}_{Ai}$ is located on the same side of the half-space to which $\boldsymbol{n}_{Bn}$ is pointing. Then, this vertex is located in the half-space defined by the face f_{Bn}. This V–F potential contact pair satisfies the half-space inclusion relation.

In the following, the detection of the E–E contact between two polyhedral blocks, Ω_A and Ω_B, is described. E_{ij} denotes an edge of Ω_A, and $\boldsymbol{v}_{Ai}$ and $\boldsymbol{v}_{Aj}$ stand for the space vectors pointing to the two vertices of this edge. f_{Ai} and f_{Aj} are the two faces, the intersection of which forms this edge. $\boldsymbol{n}_{Ai}$ denotes the inner normal vector of face f_{Ai}, and $\boldsymbol{n}_{Aj}$ stands for the inner normal vector of face f_{Aj}. Similarly, E_{kl} denotes an edge of Ω_B, and $\boldsymbol{v}_{Bk}$ and $\boldsymbol{v}_{Bl}$ stand for the space vectors pointing to the two vertices of this edge. f_{Bk} and f_{Bl} are the two faces, the intersection of which forms this edge. $\boldsymbol{n}_{Bk}$ denotes the inner normal vector of face f_{Bk}, and $\boldsymbol{n}_{Bl}$ stands for the inner normal vector of face f_{Bl}.

The two edge vectors, $\boldsymbol{h}_{Ai}$ and $\boldsymbol{h}_{Aj}$, in Figure 10 are defined as[29]

$$\begin{aligned} \boldsymbol{h}_{Ai} &= (\boldsymbol{n}_{Ai} \times \boldsymbol{n}_{Aj}) \times \boldsymbol{n}_{Ai}\,, \\ \boldsymbol{h}_{Aj} &= (\boldsymbol{n}_{Aj} \times \boldsymbol{n}_{Ai}) \times \boldsymbol{n}_{Aj}\,. \end{aligned} \tag{16}$$

10969853, 2024, 6, Downloaded from https://onlinelibrary.wiley.com/doi/10.1002/nag.3695 by Readcube (Labtiva Inc.), Wiley Online Library on [07/11/2024]. See the Terms and Conditions (https://onlinelibrary.wiley.com/terms-and-conditions) on Wiley Online Library for rules of use; OA articles are governed by the applicable Creative Commons License

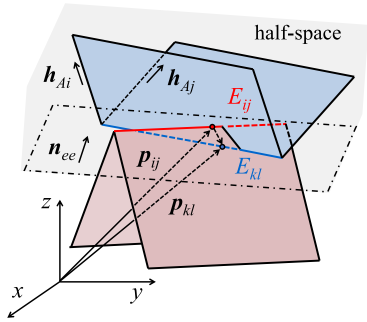

FIGURE 11 Half-space inclusion relation of an E–E potential contact pair.

The two edge vectors, $\boldsymbol{h}_{Bk}$ and $\boldsymbol{h}_{Bl}$, in Figure 10 are defined as[29]

$$\begin{aligned} \boldsymbol{h}_{Bk} &= (\boldsymbol{n}_{Bk} \times \boldsymbol{n}_{Bl}) \times \boldsymbol{n}_{Bk}\,, \\ \boldsymbol{h}_{Bl} &= (\boldsymbol{n}_{Bl} \times \boldsymbol{n}_{Bk}) \times \boldsymbol{n}_{Bl}\,. \end{aligned} \tag{17}$$

The vector $\boldsymbol{n}_{ee}$ is defined as[29]

$$\boldsymbol{n}_{ee} = \left(\boldsymbol{n}_{Ai} \times \boldsymbol{n}_{Aj}\right) \times (\boldsymbol{n}_{Bk} \times \boldsymbol{n}_{Bl})\,, \tag{18}$$

$\boldsymbol{n}_{ee}$ represents the normal vector of the plane if the edges E_{ij} and E_{kl} are in contact.

An E–E potential contact pair (see Figure 10) is defined either by the conditions

$$\begin{aligned} &\boldsymbol{n}_{ee} \times \boldsymbol{h}_{Ai} \le 0\,,\ \boldsymbol{n}_{ee} \times \boldsymbol{h}_{Aj} \le 0\,, \\ &\boldsymbol{n}_{ee} \times \boldsymbol{h}_{Bk} \ge 0\,,\ \boldsymbol{n}_{ee} \times \boldsymbol{h}_{Bl} \ge 0\,, \end{aligned} \tag{19}$$

or by the conditions

$$\begin{aligned} &\boldsymbol{n}_{ee} \times \boldsymbol{h}_{Ai} \ge 0\,,\ \boldsymbol{n}_{ee} \times \boldsymbol{h}_{Aj} \ge 0\,, \\ &\boldsymbol{n}_{ee} \times \boldsymbol{h}_{Bk} \le 0\,,\ \boldsymbol{n}_{ee} \times \boldsymbol{h}_{Bl} \le 0\,. \end{aligned} \tag{20}$$

Given a point on edge E_{ij}, defined by its space vector $\boldsymbol{p}_{ij}$, and a point on edge E_{kl}, defined by its space vector $\boldsymbol{p}_{kl}$, see Figure 11. If the direction vector $(\boldsymbol{p}_{kl} - \boldsymbol{p}_{ij})$ satisfies the condition

$$\left(\boldsymbol{p}_{kl} - \boldsymbol{p}_{ij}\right) \cdot \boldsymbol{n}_{ee} \ge 0\,, \quad \text{if} \quad \boldsymbol{n}_{ee} \times \boldsymbol{h}_{Ai} \le 0 \quad \text{and} \quad \boldsymbol{n}_{ee} \times \boldsymbol{h}_{Aj} \le 0\,, \tag{21}$$

or the condition

$$\left(\boldsymbol{p}_{kl} - \boldsymbol{p}_{ij}\right) \cdot \boldsymbol{n}_{ee} \le 0\,, \quad \text{if} \quad \boldsymbol{n}_{ee} \times \boldsymbol{h}_{Ai} \ge 0 \quad \text{and} \quad \boldsymbol{n}_{ee} \times \boldsymbol{h}_{Aj} \ge 0\,, \tag{22}$$

then the edge E_{ij} lies on the same side of the half-space to which $\boldsymbol{n}_{ee}$ is pointing. E_{ij} is located in the half-space defined by edge E_{ij} and edge E_{kl}. This E–E potential contact pair is considered to satisfy the half-space inclusion relation.

Two blocks are considered to be in contact only if all potential contact pairs between these blocks satisfy the half-space inclusion relation.

3.2.2 | Contact-type identification

After determination of the contact status by the half-space inclusion relation of potential contact pairs, the next step consists in the analysis of the specific contact type (vertex–vertex (V–V) contact, vertex–edge (V–E) contact, V–F contact, E–E contact, edge–face (E–F) contact, and face–face (F–F) contact) and the application of the corresponding contact force.

10969853, 2024, 6, Downloaded from https://onlinelibrary.wiley.com/doi/10.1002/nag.3695 by Readcube (Labtiva Inc.), Wiley Online Library on [07/11/2024]. See the Terms and Conditions (https://onlinelibrary.wiley.com/terms-and-conditions) on Wiley Online Library for rules of use; OA articles are governed by the applicable Creative Commons License

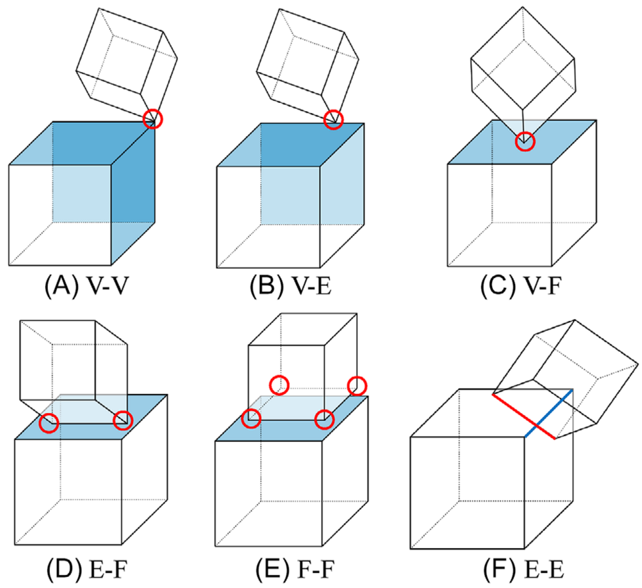

FIGURE 12 Contact types.

TABLE 5 Identification of contact types.

Contact type	V–V	V–E	V–F	E–F	F–F	E–E
Number of vertices in V–F contacts	1	1	1	2	3	0
Number of faces in V–F contacts	3	2	1	1	1	0
Number of E–E contacts	0	0	0	0	0	1

In the contact-status detection step, two blocks are defined as being in contact if all potential contact pairs satisfy the half-space inclusion relation. In the last time step before contact occurs, the potential contact pairs that do not satisfy the half-space inclusion relation are considered as contact occurrence regions. There may be one or more potential contact pairs that do not satisfy the half-space inclusion relation in the last time step before contact. Based on the number of last contact pairs, the contact type can be identified. It can be deduced from the number of V–F contacts and E–E contacts, see Figure 12.

If only one vertex in the last time step does not satisfy the half-space inclusion relation, contact occurs in this region. If there is only one face that does not satisfy the half-space inclusion relation, the contact type is V–F. If two faces do not satisfy the half-space inclusion relation, the contact type is V–E. If there are three or more faces that do not satisfy the half-space inclusion relation, the contact type is V–V.

If there are two vertices in the last noncontact step that do not satisfy the half-space inclusion relation, the contact type is E–F: either the whole edge or a part of it is in contact with a face. If three or more vertices in the last noncontact step do not satisfy the half-space inclusion relation, the contact type is F–F: either the whole face of a smaller cube is in contact with the face of a larger cube, or there is partial face–face contact with either one, two, or three vertices being actually in contact to the face. If all potential contact pairs of V–F satisfy the half-space inclusion relation, and if only potential contact pairs of E–E do not satisfy this relation, the contact type is E–E. The contact types and the corresponding number of vertices and faces in V–F contact and E–E contact are listed in Table 5.

3.2.3 | Calculation of contact forces

After detection of contact, the contact forces are calculated based on the penalty function method.[55] The position of contact between two blocks is determined, and normal and tangential contact springs are established at this position. The contact forces are calculated based on the embedding depth.

10969853, 2024, 6, Downloaded from https://onlinelibrary.wiley.com/doi/10.1002/nag.3695 by Readcube (Labtiva Inc.), Wiley Online Library on [07/11/2024]. See the Terms and Conditions (https://onlinelibrary.wiley.com/terms-and-conditions) on Wiley Online Library for rules of use; OA articles are governed by the applicable Creative Commons License

TABLE 6 Material parameters used in the numerical simulations for different sizes of cubes.

Material parameter	ρ [kg/m^3]	E [GPa]	ν	K_n, K_s [GN/m]	ζ	α_K [s]	μ_1	μ_2	μ_3
20 mm	1406.3	4.085	0.387	40.85	0.258	2.71×10^{-7}	0.262	0.305	0.274
16 mm					0.212	1.59×10^{-7}	0.271	0.316	0.287
12 mm					0.266	1.30×10^{-7}	0.314	0.358	0.303
8 mm					0.230	6.10×10^{-8}	0.443	0.444	0.356

μ_1: Friction coefficient between cubes. μ_2: Friction coefficient between cubes and the bottom plane. μ_3: Friction coefficient between cubes and the PMMA cylinder.

A linear relation between the contact forces and the embedding depth is assumed. A normal contact spring is set in the contact normal direction. The normal contact stiffness is denoted as K_n. Considering compression as positive, the normal contact force F_n is calculated as

$$F_n = -K_n \, d_n \,, \tag{23}$$

where d_n denotes the normal embedded depth.

In the following, the tangential force will be calculated. The sum of the increment of the tangential contact force and the tangential contact force of the previous time step gives the tangential contact force at the current time step. Thus, at the time instant $t+\Delta t$, the tangential contact force $F_s(t+\Delta t)$ is obtained as

$$F_s(t+\Delta t) = F_s(t) + \Delta F_s \,, \tag{24}$$

where $F_s(t)$ is the tangential contact force at the time instant t and ΔF_s denotes an increment of this force. ΔF_s is calculated as

$$\Delta F_s = K_s \, \Delta d_s \,, \tag{25}$$

where K_s stands for the tangential contact stiffness and Δd_s denotes the tangential displacement increment.

The tangential contact force is updated according to the interface friction. When the tangential contact force satisfies the inequality

$$|F_s| > \mu \, |F_n| \,, \tag{26}$$

the tangential contact force is updated to

$$|F_s| = \mu \, |F_n| \,, \tag{27}$$

where μ denotes the friction coefficient.

3.3 | Steps of simulation of the cube movement

A model with a total of 100 cubes is generated for each simulation. It consists of four cubes with a side length of 20 mm, eight cubes with 16 mm, 20 cubes with 12 mm, and 68 cubes with 8 mm. Each cube is modeled by a hexahedral element. This implies that sharp edges are simulated. The values of the normal contact stiffness, K_n, and the shear contact stiffness, K_s, are set equal to 10 times the value of the modulus of elasticity.[27] The parameters used in the numerical simulation are listed in Table 6.

The cubes are arranged either in a negative size-gradient, or in a positive size-gradient, or in a random way, see Figure 13. Taking a case from the "negative size-gradient arrangement," the process of the simulation is illustrated in Figure 14. At first, the 100 cubes of different sizes are put on top of the hollow cylinder, see Figure 14A. These cubes are moved downward by gravity. In the experiment, the cubes were inserted into the cylinder at a height of 30 cm. To simulate this situation, trying, at the same time, to save computing time, the velocities of the cubes in the simulation, when coming close to the bottom, are set equal to the theoretical value of the velocity falling from that height. The cubes get in contact with each other and stack inside the cylinder until they are stable, see Figure 14B. The cylinder moves upward at a speed of

10969853, 2024, 6, Downloaded from https://onlinelibrary.wiley.com/doi/10.1002/nag.3695 by Readcube (Labtiva Inc.), Wiley Online Library on [07/11/2024]. See the Terms and Conditions (https://onlinelibrary.wiley.com/terms-and-conditions) on Wiley Online Library for rules of use; OA articles are governed by the applicable Creative Commons License

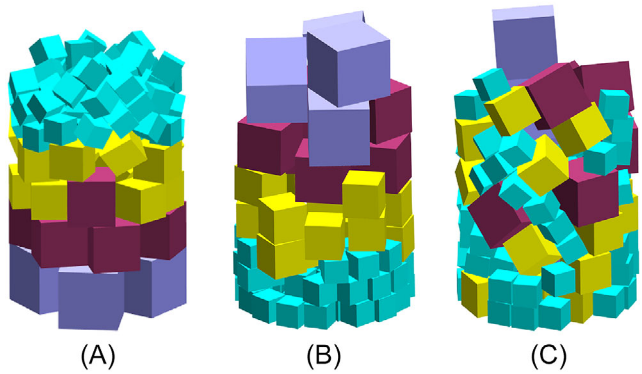

FIGURE 13 Three arrangements of cubes: (A) negative size-gradient, (B) positive size-gradient, and (C) random arrangement.

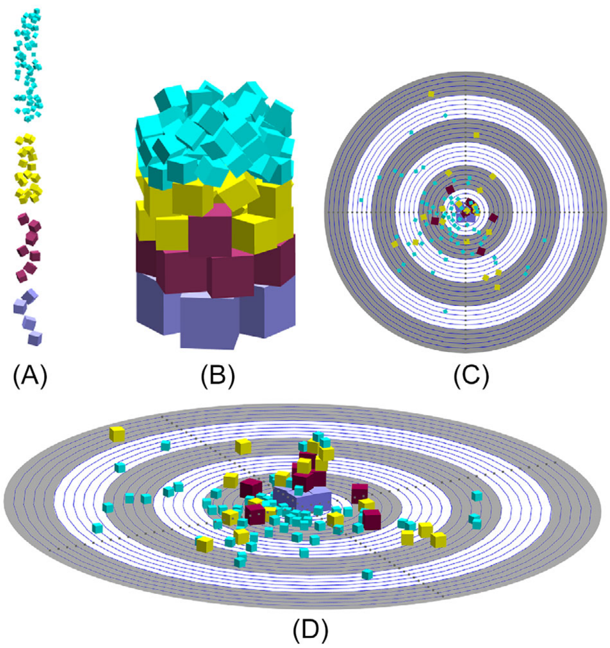

FIGURE 14 Simulation process: (A) loose cubes generated inside the confines of the cylinder, (B) initial arrangement of the cubes after stacking in the cylinder, (C) top, and (D) side view of the final positions of the cubes.

28 mm/s, and the cubes run out of the cylinder until they reach a stable final position. The positions of the dispersed cubes are documented in Figures 14C,D.

For every single simulation, the "line-up" of the cubes on top of the hollow cylinder, such as the one illustrated in Figure 14A, is newly generated. The position and the orientation of every single cube in this line-up are randomly chosen for simulations with "random arrangements," while they are only random within the size groups of the cubes for simulations referring to a size-gradient. This implies that the stable stack of cubes, obtained after having filled them into the hollow cylinder, is different in every simulation.

3.4 | Results from cube movement simulations

In each simulation, the initial configuration of the cubes is different, leading to different final dispersion results. Simulation results from the same arrangement can be quite different.

In order to identify the number of simulations, required to achieve statistically representative results, a convergence analysis was performed. This analysis was focused on "random arrangements" of the cubes. The mean values and the standard deviations of the number of cubes ending up in specific positions, obtained from 10, 20, and 40 simulations,

10969853, 2024, 6, Downloaded from https://onlinelibrary.wiley.com/doi/10.1002/nag.3695 by Readcube (Labtiva Inc.), Wiley Online Library on [07/11/2024]. See the Terms and Conditions (https://onlinelibrary.wiley.com/terms-and-conditions) on Wiley Online Library for rules of use; OA articles are governed by the applicable Creative Commons License

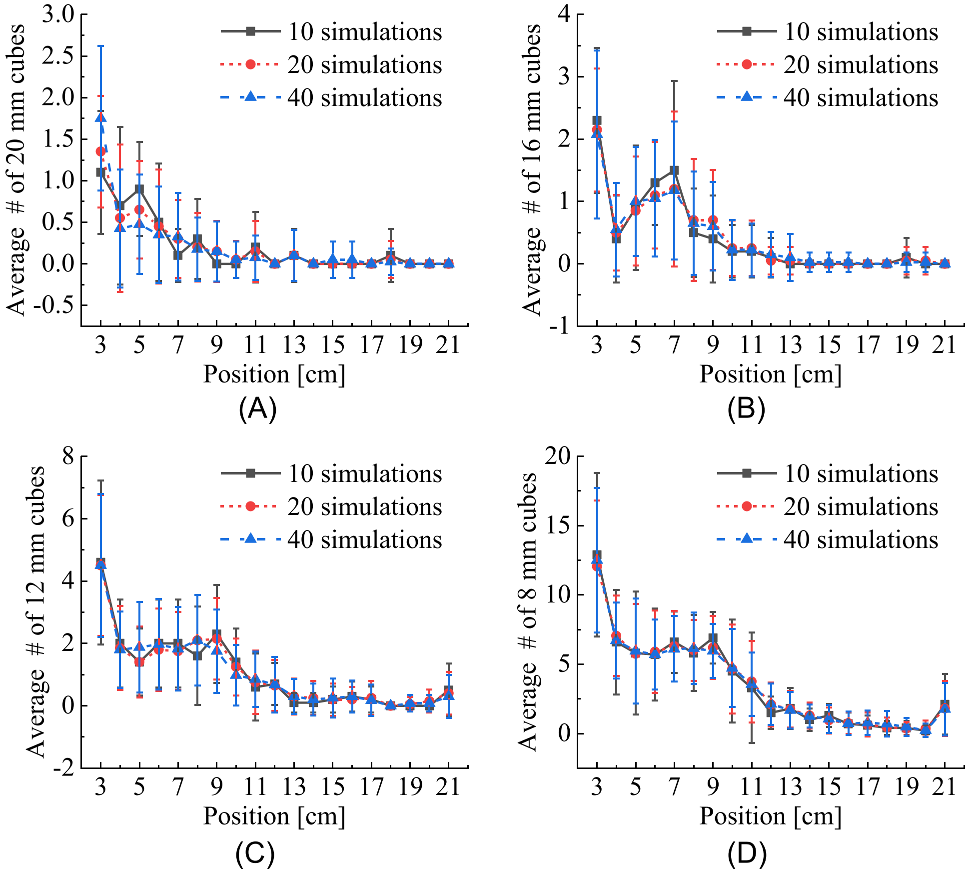

FIGURE 15 Convergence analysis of results obtained from cube movement simulations starting from initial "random arrangements" of cubes, see Table C.1: mean values and standard deviations of the number of cubes ending up in specific regions, computed on the basis of the first 10, the first 20, and all 40 simulation results: (A) 20-mm cubes, (B) 16-mm cubes, (C) 12-mm cubes, and (D) 8-mm cubes.

are shown in Figure 15. Each one of the four illustrations in Figure 15 refers to cubes of a specific size. When the number of simulations reaches 40, the mean values and the standard deviations of the cubes are close to the results for the case of 20 simulations. Thus, it is concluded that statistically representative results are achieved in this case. This is the rationale for performing 20 simulations also for the other two types of initial arrangements of the cubes, that is, for "negative size-gradient arrangements" and "positive size-gradient arrangements." The following comparison of the output of the simulations with experimental results is based on mean values and standard deviations of the first 20 simulations performed for each one of the three types of initial arrangements of the cubes.

4 | COMPARISON OF RESULTS FROM EXPERIMENTS AND SIMULATIONS

4.1 | Comparison of the results from experiments and simulations for "negative size-gradient arrangements" of cubes

In these arrangements, four sizes of cubes are dropped into the hollow cylinder, beginning with the large ones. This results in a pile with the largest cubes at the bottom and the smallest ones at the top. During upward lifting of the hollow cylinder, the cubes are running out.

From the results of the tests and the simulations, mean values and standard deviations of the positions of the cubes can be computed. The respective data for the "negative size-gradient arrangements" are listed in Appendix A. Experimental and simulation results are plotted for each size of the cubes in form of the diagrams in Figure 16, relating the number of cubes to their positions. The error bars represent the ±standard deviation from the mean value of the positions of the cubes. Figure 16A–D refers to cubes of 20, 16, 12, and 8 mm side lengths.

10969853, 2024, 6, Downloaded from https://onlinelibrary.wiley.com/doi/10.1002/nag.3695 by Readcube (Labtiva Inc.), Wiley Online Library on [07/11/2024]. See the Terms and Conditions (https://onlinelibrary.wiley.com/terms-and-conditions) on Wiley Online Library for rules of use; OA articles are governed by the applicable Creative Commons License

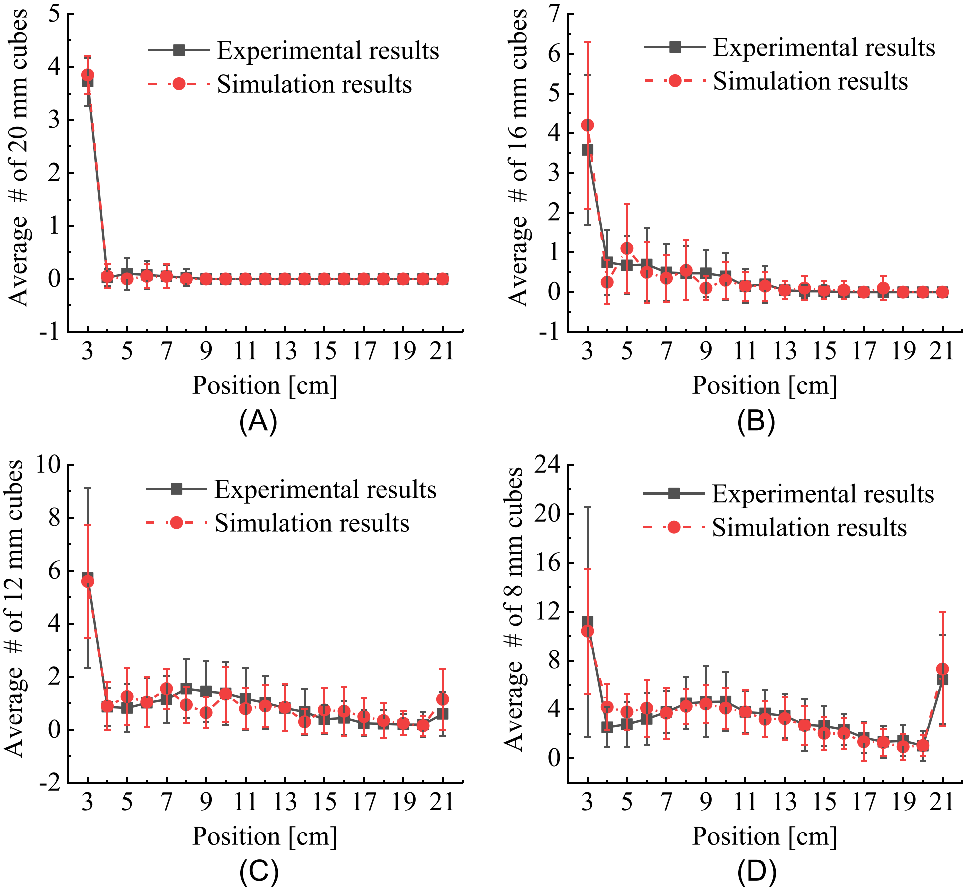

FIGURE 16 Comparison of simulation and experimental results for "negative size-gradient arrangements" of cubes, see Tables A.1 and A.2: mean values and standard deviations of the number of cubes ending up in specific regions: (A) 20-mm cubes, (B) 16-mm cubes, (C) 12-mm cubes, and (D) 8-mm cubes.

TABLE 7 Correlation values of simulation and experimental results for "negative size-gradient arrangements" of cubes.

Side length of cubes [mm]	20	16	12	8
Correlation values	0.101	0.271	0.241	0.124

The 20-mm cubes are almost all inside a radius of 3 cm from the center, because they are placed at the bottom of the cylinder. They hardly move after lifting the cylinder. The 16-mm cubes are inside a radius of 18 cm from the center. The 12-mm cubes and the 8-mm cubes move to a distance of more than 20 cm from the center. Disregarding cubes inside a radius of 3 cm and outside a radius of 21 cm, most of the 12 and 8-mm cubes are located at a distance of 8–10 cm from the center point of the circles.

To improve the comprehensibility of the comparison, the correlations between the experimental and the simulated data are evaluated by the ratio of the area between the lines of experimental and simulated results. The expression of the correlation value, A_D/A_E, is given as follows:

$$\frac{A_D}{A_E} = \frac{\sum_{x=3}^{20} \int_x^{x+1} |f(x) - g(x)| \, \mathrm{d}x}{\sum_{x=3}^{20} \int_x^{x+1} f(x) \, \mathrm{d}x}. \tag{28}$$

A_D denotes the area between the line of the experimental results and the one of the simulation results. A_E denotes the area under the line of the experimental results. The position of the cubes is denoted as x. $f(x)$ stands for the experimental results, and $g(x)$ denotes the simulation results. The closer the value is to 0, the better the correlation of the results.

The correlation values for the "negative size-gradient arrangements" are listed in Table 7. The correlation values for cubes with side lengths of 20 and 8 mm are smaller than for cubes with side lengths of 16 and 12 mm. This indicates that

10969853, 2024, 6, Downloaded from https://onlinelibrary.wiley.com/doi/10.1002/nag.3695 by Readcube (Labtiva Inc.), Wiley Online Library on [07/11/2024]. See the Terms and Conditions (https://onlinelibrary.wiley.com/terms-and-conditions) on Wiley Online Library for rules of use; OA articles are governed by the applicable Creative Commons License

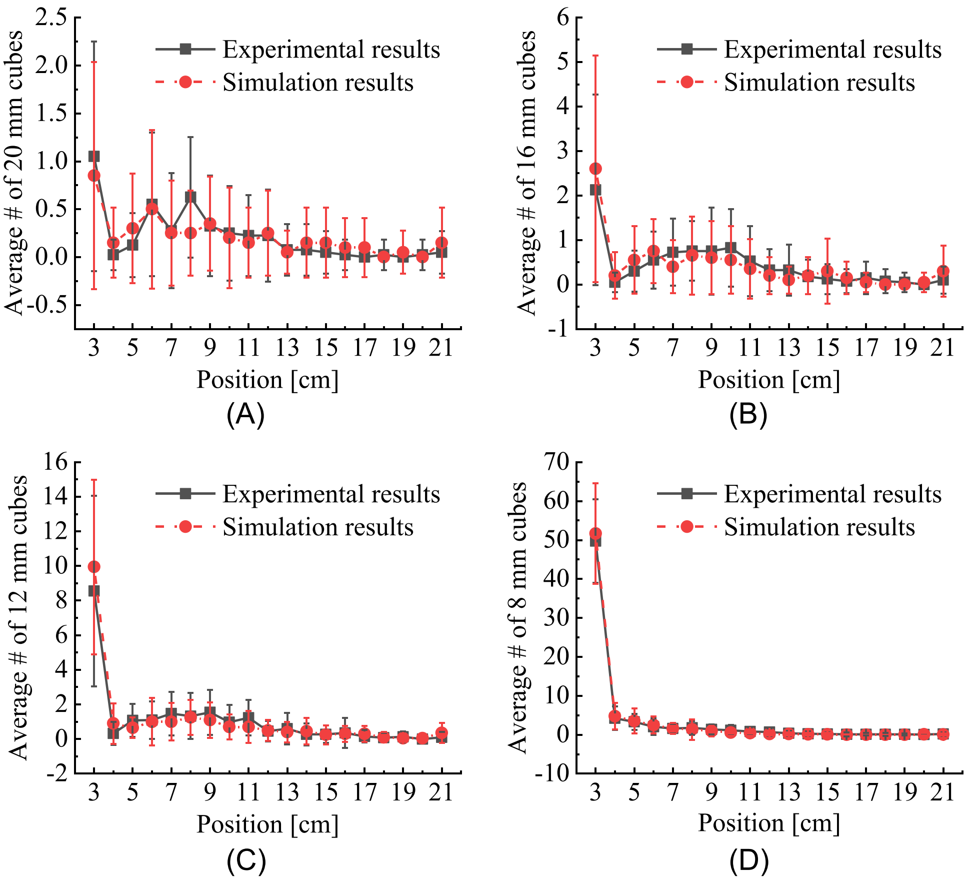

FIGURE 17 Comparison of simulation and experimental results for “positive size-gradient arrangements” of cubes, see Tables B.1 and B.2: mean values and standard deviations of the number of cubes ending up in specific regions: (A) 20-mm cubes, (B) 16-mm cubes, (C) 12-mm cubes, and (D) 8-mm cubes.

the results are more consistent for the size of the cubes located at the bottom (20 mm) and for the size of the cubes with the greatest number (8 mm).

4.2 | Comparison of the results from experiments and simulations for “positive size-gradient arrangements” of cubes

In these arrangements, four sizes of cubes are dropped into the hollow cylinder, beginning with the small ones. This results in a pile with the smallest cubes at the bottom and the largest ones at the top.

The respective data for the “positive size-gradient arrangements” are listed in Appendix B. Experimental and simulation results are plotted for each size of the cubes in form of the diagrams in Figure 17, relating the number of cubes to their positions. Figures 17A–D refer to cubes of 20, 16, 12, and 8 mm side lengths.

Because of the impact effect of larger cubes falling onto smaller ones, the 8-mm cubes form a stable pile, with more than 73% of them ending up inside a radius of 3 cm from the center. Compared to the “negative size-gradient arrangements,” there are more 12-mm cubes located inside a radius of 3 cm in the “positive size-gradient arrangements” of cubes. However, the 20 and 16-mm cubes are moving farther than in the “negative size-gradient arrangements.” Disregarding cubes inside a radius of 3 cm and outside one of 21 cm, most of the 20 and 12-mm cubes are located at a distance of 6–11 cm from the center point of the circles.

The correlation values for “positive size-gradient arrangements” of cubes are listed in Table 8. In the “positive size-gradient arrangements,” the correlation is the better, the smaller the size of the cubes, because the smaller cubes are located under the larger ones, and there are more cubes of smaller size. The increase in the number of cubes improves the statistical significance of the results.

10969853, 2024, 6, Downloaded from https://onlinelibrary.wiley.com/doi/10.1002/nag.3695 by Readcube (Labtiva Inc.), Wiley Online Library on [07/11/2024]. See the Terms and Conditions (https://onlinelibrary.wiley.com/terms-and-conditions) on Wiley Online Library for rules of use; OA articles are governed by the applicable Creative Commons License

TABLE 8 Correlation values of simulation and experimental results for "positive size-gradient arrangements" of cubes.

Side length of cubes [mm]	20	16	12	8
Correlation values	0.368	0.384	0.255	0.124

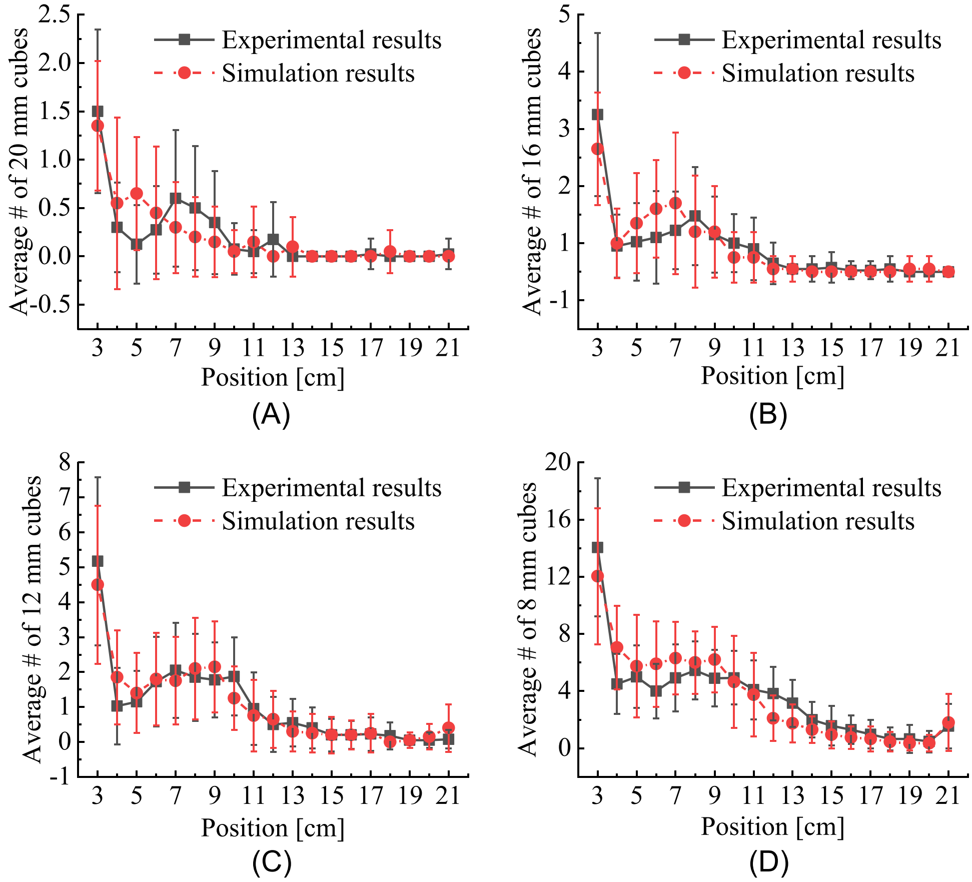

FIGURE 18 Comparison of simulation and experimental results for "random arrangements" of cubes, see Tables C.1 and C.2: mean values and standard deviations of the number of cubes ending up in specific regions: (A) 20-mm cubes, (B) 16-mm cubes, (C) 12-mm cubes, and (D) 8-mm cubes.

4.3 | Comparison of the results from experiments and simulations for "random arrangements" of cubes

For such arrangements, four sizes of cubes are well mixed before being dropped into the hollow cylinder. This results in a pile with a random distribution of cubes.

The respective data for the "random arrangements" are listed in Appendix C. Experimental and simulation results are plotted for each size of the cubes in form of the diagrams in Figure 18, relating the number of cubes to their positions. Figure 18A–D refers to cubes of 20, 16, 12, and 8-mm side lengths.

Since the cubes are randomly arranged, their final distributions are irregular. It can be seen that most of the cubes are located inside a radius of 15 cm from the center. Only a few cubes are located outside a radius of more than 20 cm from the center. Except for the cubes located inside a radius of 3 cm, most of the cubes are located at a distance of 7–10 cm from the center point of the circles.

The correlation values for "random arrangements" of cubes are listed in Table 9. Cubes with side lengths of 12 and 8 mm have better correlations because there are more cubes of these two sizes. The correlation value for cubes with side lengths of 20 mm is greater than the one for other sizes, because the number of cubes of 20-mm side length is small. This reduces the rate of convergence of the results for cubes of this size.

10969853, 2024, 6, Downloaded from https://onlinelibrary.wiley.com/doi/10.1002/nag.3695 by Readcube (Labtiva Inc.), Wiley Online Library on [07/11/2024]. See the Terms and Conditions (https://onlinelibrary.wiley.com/terms-and-conditions) on Wiley Online Library for rules of use; OA articles are governed by the applicable Creative Commons License

TABLE 9 Correlation values of simulation and experimental results for "random arrangements" of cubes.

Side length of cubes [mm]	20	16	12	8
Correlation values	0.600	0.373	0.189	0.244

5 DISCUSSION

All experiments were carried out with the same 100 cubes of different sizes. This limitation to 100 cubes renders the question regarding possible scaling effects, associated with *different number* of cubes of different sizes, open for future research. Larger tests might be associated with smaller randomness and uncertainty, but also the efforts needed for the documentation of the results would increase significantly.

The stable stack of cubes obtained after filling them into the hollow cylinder exhibited at least a rough order of sizes in the experiments and simulations referring to either a positive or a negative size-gradient. Still, every single experiment and every single simulation was, strictly speaking, started from a *unique* stable stack of cubes. Therefore, it would be questionable to compare results from one specific experiment with results from one specific simulation. Instead, many very similar but not strictly identical tests were performed and evaluated statistically. These results were compared with those from the statistical evaluation of many very similar but not strictly identical simulations. This approach is useful for the demonstration of the randomness and the uncertainty associated with both the experiments and the simulations.

The here-used CDEM is an extension of its predecessor.[29] The two methods differ in the approach used for determination of the contact type. Formally, this identification was based on the location of the contact point.[29] In the present study, the approach was further improved by using the location and the number of contact pairs, which satisfy the half-space inclusion relation in the previous step of the explicit simulation.

Since the cubes did not break during the experiments, not only the CDEM but also other approaches for the simulation of particle movement and interaction are well suited for the analysis of the cube movement tests, for example, the Universal Distinct Element Code (UDEC) and the three-dimensional Distinct Element Code (3DEC).[67] UDEC/3DEC is mainly based on the finite difference method and uses mixed discretizations with different element types. In CDEM, the blocks are represented by means of finite elements, and an explicit solution scheme based on the dynamic relaxation method is used. Thus, CDEM is particularly well suited for the simulation of problems in which the deformation of continuous bodies is important.

6 SUMMARY AND CONCLUSIONS

In this work, a test was designed to study the movement of cubes of different size. An improved contact-pairs-based contact-detection algorithm for polyhedral blocks was used. Then, employing the contact algorithm, the dispersion of cubes of different size and with different arrangements was simulated and compared with the experimental results. Three different arrangements of cubes were used, namely, a negative size-gradient, a positive size-gradient, and a random arrangement. The main conclusions of the presented work are as follows:

1. The initial structure of the cubes inside the hollow cylinder differed each time. Forty experiments were carried out for each one of the three types of initial cube arrangements. A convergence analysis revealed that 20 tests are enough to obtain statistically relevant results. A similar convergence analysis was performed with the simulation tool. This analysis focused on the initial "random arrangement" of the cubes. It was found that 20 simulations are enough to obtain statistically relevant results. Thus, there is an agreement of experimental and numerical findings.
2. The contact type can be determined through the location and the number of contact pairs that satisfy the half-space inclusion relationship before the contact step. By adopting the linear spring-dashpot contact model, the stiffness proportional damping coefficient for Rayleigh damping was determined by testing the coefficients of restitution of the cubes.
3. "Positive size-gradient arrangements" resulted in the smallest range of movement compared to "negative size-gradient arrangements" and "random arrangements." The number of larger cubes (i.e., cubes with 20 and 16-mm side lengths) used in this study was quite small. Still, the interaction of few larger cubes with many more smaller cubes had a significant influence on the test results.

10969853, 2024, 6, Downloaded from https://onlinelibrary.wiley.com/doi/10.1002/nag.3695 by Readcube (Labtiva Inc.), Wiley Online Library on [07/11/2024]. See the Terms and Conditions (https://onlinelibrary.wiley.com/terms-and-conditions) on Wiley Online Library for rules of use; OA articles are governed by the applicable Creative Commons License

4. The here-reported experiments with cubes of different sizes enrich the existing pool of benchmark tests regarding particle movement and interaction problems. They represent another nontrivial validation example for the quantitative assessment of related simulation approaches. Provided that such a software is capable of reproducing the here-reported experimental results, it is further corroborated.

ACKNOWLEDGMENTS

The authors gratefully acknowledge the financial support provided by the China Scholarship Council (CSC) and the National Key Research and Development Project of China, the Ministry of Science and Technology of China (Project No. 2018YFC1505504). Finally, the authors acknowledge TU Wien Bibliothek for financial support through its Open Access Funding Program.

CONFLICT OF INTEREST STATEMENT

The authors declare no conflicts of interest.

DATA AVAILABILITY STATEMENT

Data will be made available by the authors upon reasonable request.

ORCID

Xinquan Wang https://orcid.org/0000-0001-8081-0078
Chun Feng https://orcid.org/0000-0001-6592-144X
Yiming Zhang https://orcid.org/0000-0002-3693-8039
Bernhard L. A. Pichler https://orcid.org/0000-0002-6468-1840

REFERENCES

1. Glade T, Anderson MG, Crozier MJ. *Landslide Hazard and Risk*. Vol 807. John Wiley & Sons; 2005.
2. Takahashi T. *Debris Flow: Mechanics, Prediction and Countermeasures*. Taylor & Francis; 2007
3. Cundall PA, Strack ODL. A discrete numerical model for granular assemblies. *Geotechnique*. 1979;29(1):47-65. 10.1680/geot.1979.29.1.47
4. Shi G. Discontinuous deformation analysis: a new numerical model for the statics and dynamics of deformable block structures. *Eng Comput*. 1992;9 (2):157-168. 10.1108/eb023855
5. Fan H, Wang J, Zheng H. Variational inequality-based particle discontinuous deformation analysis. *Int J Numer Anal Methods Geomech*. 2019;43 (11):1995-2019. 10.1002/nag.2942
6. Yang Y, Guo H, Fu X, Zheng H. Boundary settings for the seismic dynamic response analysis of rock masses using the numerical manifold method. *Int J Numer Anal Methods Geomech*. 2018;42 (9):1095-1122. 10.1002/nag.2786
7. Ma GW, An XM, Zhang HH, Li LX. Modeling complex crack problems using the numerical manifold method. *Int J Fract*. 2009;156 (1):21-35. 10.1007/s10704-009-9342-7
8. Bardenhagen SG, Brackbill JU, Sulsky D. The material-point method for granular materials. *Comput Methods Appl Mech Eng*. 2000;187 (3-4):529-541. 10.1016/s0045-7825(99)00338-2
9. Bandara S, Ferrari A, Laloui L. Modelling landslides in unsaturated slopes subjected to rainfall infiltration using material point method. *Int J Numer Anal Methods Geomech*. 2016;40 (9):1358-1380. 10.1002/nag.2499
10. Gingold RA, Monaghan JJ. Smoothed particle hydrodynamics: theory and application to non-spherical stars. *Mon Not R Astron Soc*. 1977;181 (3):375-389. 10.1093/mnras/181.3.375
11. Pastor M, Yague A, Stickle MM, Manzanal D, Mira P. A two-phase SPH model for debris flow propagation. *Int J Numer Anal Methods Geomech*. 2018;42 (3):418-448. 10.1002/nag.2748
12. Munjiza A, Owen D, Bicanic N. A combined finite-discrete element method in transient dynamics of fracturing solids. *Eng Comput*. 1995. 10.1108/02644409510799532
13. Li S, Zhao M, Wang Y, Rao Y. A new numerical method for DEM–block and particle model. *Int J Rock Mech Min Sci*. 2004;41:414-418. 10.1016/j.ijrmms.2004.03.076
14. Li S, Tang D, Wang J. A two-scale contact model for collisions between blocks in CDEM. *Sci China Technol Sci*. 2015;58 (9):1596-1603. 10.1007/s11431-015-5902-4
15. Zhao T, Xu G, Zhou Y, Huang Z, Xue JDu L,. CDEM simulation of top-coal caving characteristics under synchronous multiwindow drawing in longwall top-coal caving mining of extra-thick coal seam. *Energy Sci Eng*. 2022;10 (9):3617-3637. 10.1002/ese3.1245
16. Ren Q, Zhao Y, Zhu X, et al. CDEM-based simulation of the 3D propagation of hydraulic fractures in heterogeneous Coalbed Methane reservoirs. *Comput Geotech*. 2022;152:104992. 10.1016/j.compgeo.2022.104992
17. Zhu X, Feng C, Cheng P, Wang X, Li S. A novel three-dimensional hydraulic fracturing model based on continuum–discontinuum element method. *Comput Methods Appl Mech Eng*. 2021;383:113887. 10.1016/j.cma.2021.113887

10969853, 2024, 6, Downloaded from https://onlinelibrary.wiley.com/doi/10.1002/nag.3695 by Readcube (Labtiva Inc.), Wiley Online Library on [07/11/2024]. See the Terms and Conditions (https://onlinelibrary.wiley.com/terms-and-conditions) on Wiley Online Library for rules of use; OA articles are governed by the applicable Creative Commons License

18. Yue Z, Zhou J, Feng C, Wang X, Peng L, Cong J. Coupling of material point and continuum discontinuum element methods for simulating blast-induced fractures in rock. *Comput Geotech*. 2022;144:104629. 10.1016/j.compgeo.2021.104629
19. Ding C, Yang R, Feng C. Stress wave superposition effect and crack initiation mechanism between two adjacent boreholes. *Int J Rock Mech Min Sci*. 2021;138:104622. 10.1016/j.ijrmms.2021.104622
20. Zhou J, Yue Z, Feng C, Wang P, Yue X, Tao T. Experiments and numerical simulations on dynamic crack behavior at the interface of layered brittle material. *Fatigue Fract Eng Mater Struct*. 2022;45 (12):3546-3558. 10.1111/ffe.13829
21. Feng C, Liu X, Lin Q, Li S. A simple particle–spring method for capturing the continuous–discontinuous processes of brittle materials. *Eng Anal Bound Elem*. 2022;139:221-231. 10.1016/j.enganabound.2022.03.015
22. Tang H, Ji X, Zhang H, Li T. Numerical simulation of large compression deformation disaster and supporting behavior of deep buried soft rock tunnel with high in situ stress based on CDEM. *Adv Civ Eng*. 2022;2022:1-13. 10.1155/2022/5985165
23. Feng C, Li S, Liu T, Wang X, Zhu X. Numerical-simulation-based landslide warning system and its application. *IOP Conf Ser Earth Environ Sci*. 2021;861 (6):062025. 10.1088/1755-1315/861/6/062025
24. Gao M, Zhang H, Cui S, et al. Investigation on deformation mechanism and treatment effect of a scattered slope based on continuum–discontinuum element method and finite difference method. *Front Earth Sci*. 2022;10:894923. 10.3389/feart.2022.894923
25. Zhao J, Zhao S, Luding S. The role of particle shape in computational modelling of granular matter. *Nat Rev Phys*. 2023;5 (9):505-525. 10.1038/s42254-023-00617-9
26. Liu XL, Lemos JV. Procedure for contact detection in discrete element analysis. *Adv Eng Softw*. 2001;32 (5):409-415. 10.1016/S0965-9978(00)00101-0
27. Wang J, Li S, Feng C. A shrunken edge algorithm for contact detection between convex polyhedral blocks. *Comput Geotech*. 2015;63:315-330. 10.1016/j.compgeo.2014.10.009
28. Feng C, Li S, Liu X, Zhang Y. A semi-spring and semi-edge combined contact model in CDEM and its application to analysis of Jiweishan landslide. *J Rock Mech Geotech Eng*. 2014;6 (1):26-35. 10.1016/j.jrmge.2013.12.001
29. Wang X, Feng C, Zhu X, Zhang L, Li S. A half-space based contact detection algorithm for complex blocks. *Comput Geotech*. 2021;135:104168. 10.1016/j.compgeo.2021.104168
30. Kheradmand E, Prudhomme S, Laforest M. A fast contact detection method for ellipsoidal particles. *Int J Numer Anal Methods Geomech*. 2021;45 (9):1169-1194. 10.1002/nag.3197
31. Cundall PA. Formulation of a three-dimensional distinct element model—part I. A scheme to detect and represent contacts in a system composed of many polyhedral blocks. *Int J Rock Mech Min Sci Geomech Abstracts*. 1988;25 (3):107-116. 10.1016/0148-9062(88)92293-0
32. Nezami EG, Hashash YMA, Zhao D, Ghaboussi J. A fast contact detection algorithm for 3-D discrete element method. *Comput Geotech*. 2004;31 (7):575-587. 10.1016/j.compgeo.2004.08.002
33. Nezami GE, Hashash MAY, Zhao D, Ghaboussi J. Shortest link method for contact detection in discrete element method. *Int J Numer Anal Methods Geomech*. 2006;30 (8):783-801. 10.1002/nag.500
34. Chang SW, Chen CS. A non-iterative derivation of the common plane for contact detection of polyhedral blocks. *Int J Numer Methods Eng*. 2008;74 (5):734-753. 10.1002/nme.2174
35. Vorobiev O. Simple common plane contact algorithm. *Int J Numer Methods Eng*. 2012;90 (2):243-268. 10.1002/nme.3324
36. Shi G. Contact theory. *Sci China Technol Sci*. 2015;58 (9):1450-1496. 10.1007/s11431-015-5814-3
37. Wang X, Wu W, Zhu H, Zhang H, Lin JS, Bobet A. A global direct search method for high-fidelity contact detection between arbitrarily shaped three-dimensional convex polyhedral blocks. *Comput Geotech*. 2022;150:104891. 10.1016/j.compgeo.2022.104891
38. Zhuang X, Zheng F, Zheng H, Jiao Y, Rabczuk T, Wriggers P. A cover-based contact detection approach for irregular convex polygons in discontinuous deformation analysis. *Int J Numer Anal Methods Geomech*. 2021;45 (2):208-233. 10.1002/nag.3157
39. Zheng F, Jiao YY, Zhang XL, Tan F, Wang L, Zhao Q. Object-oriented contact detection approach for three-dimensional discontinuous deformation analysis based on entrance block theory. *Int J Geomech*. 2017;17 (5):E4016009. 10.1061/(asce)gm.1943-5622.0000718
40. Yan CZ, Zheng H. A new potential function for the calculation of contact forces in the combined finite-discrete element method. *Int J Numer Anal Methods Geomech*. 2017;41 (2):265-283. 10.1002/nag.2559
41. Zheng F, Zhuang X, Zheng H, Jiao YY, Rabczuk T. Kinetic analysis of polyhedral block system using an improved potential-based penalty function approach for explicit discontinuous deformation analysis. *Appl Math Model*. 2020;82:314-335. 10.1016/j.apm.2020.01.026
42. Zheng F, Zhuang X, Zheng H, Jiao YY, Rabczuk T. A robust potential-based contact force solution approach for discontinuous deformation analysis of irregular convex polygonal block/particle systems. *Acta Geotech*. 2020;16:679-697. 10.1007/s11440-020-00997-7
43. Gui N, Yang X, Jiang S, Tu J, Fan J. Extended HPM-DEM coupled simulation of drainage of square particles in a 2D Hopper flow. *AIChE J*. 2016;62 (6):1863-1876.
44. Jean M. The non-smooth contact dynamics method. *Comput Methods Appl Mech Eng*. 1999;177 (3-4):235-257. 10.1016/s0045-7825(98)00383-1
45. Glocker C, Pfeiffer F. Dynamical systems with unilateral contacts. *Nonlinear Dyn*. 1992;3 (4):245-259. 10.1007/bf00045484
46. Esen O, Lainz Valcázar M, De León M, Sardón C. Implicit contact dynamics and Hamilton-Jacobi theory. *Differ Geom Appl*. 2023;90:102030. 10.1016/j.difgeo.2023.102030
47. Azevedo NM, Lemos J, Almeida dJR. Influence of aggregate deformation and contact behaviour on discrete particle modelling of fracture of concrete. *Eng Fract Mech*. 2008;75 (6):1569-1586.
48. Hughes TJR, Taylor RL, Sackman JL, Curnier A, Kanoknukulchai W. A finite element method for a class of contact-impact problems. *Comput Methods Appl Mech Eng*. 1976;8 (3):249-276.

10969853, 2024, 6, Downloaded from https://onlinelibrary.wiley.com/doi/10.1002/nag.3695 by Readcube (Labtiva Inc.), Wiley Online Library on [07/11/2024]. See the Terms and Conditions (https://onlinelibrary.wiley.com/terms-and-conditions) on Wiley Online Library for rules of use; OA articles are governed by the applicable Creative Commons License

49. Bayo E, Garcia De Jalon J, Serna MA. A modified Lagrangian formulation for the dynamic analysis of constrained mechanical systems. *Comput Methods Appl Mech Eng*. 1988;71 (2):183-195.
50. Ruiz-Carulla R, Corominas J, Mavrouli O. A methodology to obtain the block size distribution of fragmental rockfall deposits. *Landslides*. 2015;12 (4):815-825. 10.1007/s10346-015-0600-7
51. Siman-Tov S, Katz O, Matmon A. Examining the effects of ground motion and rock strength on the size of boulders falling from an overhanging cliff. *Eng Geol*. 2017;220:164-174. 10.1016/j.enggeo.2017.02.008
52. Derakhshani SM, Schott DL, Lodewijks G. Micro-macro properties of quartz sand: experimental investigation and DEM simulation. *Powder Technol*. 2015;269:127-138. 10.1016/j.powtec.2014.08.072
53. Hamed A, Xia Y, Saha N, Klinger J, Lanning DN, Dooley J. Flowability of crumbler rotary shear size-reduced granular biomass: an experiment-informed modeling study on the angle of repose. *Front Energy Res*. 2022;10. 10.3389/fenrg.2022.859248
54. Beakawi Al-Hashemi HM, Baghabra Al-Amoudi OS. A review on the angle of repose of granular materials. *Powder Technol*. 2018;330:397-417. 10.1016/j.powtec.2018.02.003
55. Wriggers P. *Computational Contact Mechanics*. Springer; 2006
56. Ferraris CF. Measurement of the rheological properties of high performance concrete: state of the art report. *J Res Natl Inst Stand Technol*. 1999;104 (5):461-478. 10.6028/jres.104.028
57. Choi MS, Lee JS, Ryu KS, Koh KT, Kwon SH. Estimation of rheological properties of UHPC using mini slump test. *Constr Build Mater*. 2016;106:632-639. 10.1016/j.conbuildmat.2015.12.106
58. Zhou ZY, Zou RP, Pinson D, Yu AB. Angle of repose and stress distribution of sandpiles formed with ellipsoidal particles. *Granul Matter*. 2014;16 (5):695-709. 10.1007/s10035-014-0522-4
59. Irfan-ul-Hassan M, Pichler B, Reihsner R, Hellmich C. Elastic and creep properties of young cement paste, as determined from hourly repeated minute-long quasi-static tests. *Cem Concr Res*. 2016;82:36-49. 10.1016/j.cemconres.2015.11.007
60. Kohlhauser C, Hellmich C. Ultrasonic contact pulse transmission for elastic wave velocity and stiffness determination: influence of specimen geometry and porosity. *Eng Struct*. 2013;47:115-133. 10.1016/j.engstruct.2012.10.027
61. Franck A. *Kunststoff-Kompendium*. Vogel Verlag; 2000.
62. Li T, Zhang J, Ge W. Simple measurement of restitution coefficient of irregular particles. *China Part*. 2004;2 (6):274-275. 10.1016/S1672-2515(07)60074-8
63. Benson DJ. Computational methods in Lagrangian and Eulerian hydrocodes. *Comput Methods Appl Mech Eng*. 1992;99 (2):235-394. 10.1016/0045-7825(92)90042-I
64. Liu M, Gorman DG. Formulation of Rayleigh damping and its extensions. *Comput Struct*. 1995;57 (2):277-285. 10.1016/0045-7949(94)00611-6
65. Shaefer J, Dippel S, Wolf D. Force schemes in simulations of granular materials. *J Phys I*. 1996;6 (1):5-20. 10.1051/jp1:1996129
66. Cleary PW. Predicting charge motion, power draw, segregation and wear in ball mills using discrete element methods. *Miner Eng*. 1998;11 (11):1061-1080. 10.1016/S0892-6875(98)00093-4
67. Israelsson JI. Short descriptions of UDEC and 3DEC. In: Developments in Geotechnical Engineering. Vol 79. Elsevier; 1996:523-528.

How to cite this article: Wang X, Feng C, Lahayne O, Zhang Y, Mang HA, Pichler BLA. A new cube movement test for verification of simulations of contact processes of blocks of different size in geological hazards. *Int J Numer Anal Methods Geomech*. 2024;48:1553–1580. https://doi.org/10.1002/nag.3695

APPENDIX A: DATA FOR NEGATIVE SIZE-GRADIENT CASES

The mean values and the standard deviations of the positions of the cubes, based on 20 simulations with “negative size-gradient arrangements,” are listed in Table A.1. The mean values and the standard deviations of the positions of the cubes, based on 40 experiments with “negative size-gradient arrangements”, are listed in Table A.2.

The first column refers to the position of the cube. It is defined as the distance from the center point of the cube to the one of the circles on the bottom plane. The center point of the cube is the point obtained by projecting its center of gravity onto the bottom plane.

A position of 3 cm means that the distance from the center point of the cube to the one of the circles is less than 3 cm. Thus, if the distance from the center point of the cube to the one of the circles is less than 3 cm, this cube is assigned to the group of position 3 cm. A position of 4 cm means that the distance from the center point of the cube to the one of the circles is greater than 3 cm, but less than 4 cm. The positions 5–20 cm have a similar meaning. A position of 21 cm means that the distance from the center point of the cube to the one of the circles is greater than 20 cm. Columns 2–5 contain the mean values of cubes with side lengths of 20 , 16 , 12 , and 8 mm in the respective position. Columns 6–9 contain the standard deviation of the mean value of cubes with side lengths of 20 , 16 , 12 , and 8 mm at these positions. The tables in Appendices B and C have the same structure.

10969853, 2024, 6, Downloaded from https://onlinelibrary.wiley.com/doi/10.1002/nag.3695 by Readcube (Labtiva Inc.), Wiley Online Library on [07/11/2024]. See the Terms and Conditions (https://onlinelibrary.wiley.com/terms-and-conditions) on Wiley Online Library for rules of use; OA articles are governed by the applicable Creative Commons License

TABLE A.1 Mean value and standard deviation of the positions of the cubes, based on 20 negative size-gradient simulations.

Position [cm]	Mean value				Standard deviation			
	20 mm	16 mm	12 mm	8 mm	20 mm	16 mm	12 mm	8 mm
3	3.850	4.200	5.600	10.400	0.366	2.093	2.137	5.113
4	0.050	0.250	0.900	4.200	0.224	0.550	0.912	1.908
5	0.000	1.100	1.250	3.800	0.000	1.119	1.070	1.473
6	0.050	0.500	1.050	4.100	0.224	0.761	0.945	2.315
7	0.050	0.350	1.550	3.700	0.224	0.587	0.759	2.105
8	0.000	0.550	0.950	4.250	0.000	0.759	0.686	1.446
9	0.000	0.100	0.650	4.450	0.000	0.308	0.587	1.538
10	0.000	0.300	1.350	4.100	0.000	0.470	1.040	1.68
11	0.000	0.150	0.800	3.800	0.000	0.366	0.768	1.79
12	0.000	0.150	0.900	3.200	0.000	0.366	0.788	1.47
13	0.000	0.050	0.850	3.250	0.000	0.224	0.875	1.74
14	0.000	0.100	0.300	2.700	0.000	0.308	0.470	1.59
15	0.000	0.050	0.750	2.050	0.000	0.224	0.851	1.35
16	0.000	0.050	0.700	2.050	0.000	0.224	0.923	1.27
17	0.000	0.000	0.500	1.350	0.000	0.000	0.688	1.53
18	0.000	0.100	0.350	1.300	0.000	0.308	0.671	1.12
19	0.000	0.000	0.250	0.950	0.000	0.000	0.444	1.05
20	0.000	0.000	0.150	1.050	0.000	0.000	0.366	0.88
21	0.000	0.000	1.150	7.300	0.000	0.000	1.137	4.68

TABLE A.2 Mean value and standard deviation of the positions of the cubes, based on 40 negative size-gradient experiments.

Position [cm]	Mean value				Standard deviation			
	20 mm	16 mm	12 mm	8 mm	20 mm	16 mm	12 mm	8 mm
3	3.725	3.575	5.725	11.175	0.452	1.880	3.389	9.391
4	0.025	0.750	0.875	2.550	0.158	0.809	0.723	1.632
5	0.100	0.675	0.825	2.800	0.304	0.730	0.903	1.829
6	0.075	0.700	1.025	3.225	0.267	0.911	0.920	2.106
7	0.050	0.500	1.150	3.800	0.221	0.716	0.893	1.713
8	0.025	0.475	1.550	4.500	0.158	0.679	1.108	2.124
9	0.000	0.475	1.450	4.625	0.000	0.599	1.154	2.888
10	0.000	0.400	1.375	4.650	0.000	0.591	1.192	2.445
11	0.000	0.150	1.175	3.800	0.000	0.427	1.174	1.698
12	0.000	0.200	1.025	3.675	0.000	0.464	1.000	1.927
13	0.000	0.050	0.825	3.475	0.000	0.221	0.874	1.797
14	0.000	0.025	0.675	2.750	0.000	0.158	0.859	2.097
15	0.000	0.025	0.400	2.650	0.000	0.158	0.545	1.610
16	0.000	0.000	0.450	2.350	0.000	0.000	0.639	1.272
17	0.000	0.000	0.250	1.700	0.000	0.000	0.494	1.285
18	0.000	0.000	0.225	1.350	0.000	0.000	0.530	1.272
19	0.000	0.000	0.200	1.450	0.000	0.000	0.405	1.280
20	0.000	0.000	0.200	1.025	0.000	0.000	0.464	1.209
21	0.000	0.000	0.600	6.450	0.000	0.000	0.841	3.623

10969853, 2024, 6, Downloaded from https://onlinelibrary.wiley.com/doi/10.1002/nag.3695 by Readcube (Labtiva Inc.), Wiley Online Library on [07/11/2024]. See the Terms and Conditions (https://onlinelibrary.wiley.com/terms-and-conditions) on Wiley Online Library for rules of use; OA articles are governed by the applicable Creative Commons License

APPENDIX B: DATA FOR POSITIVE SIZE-GRADIENT CASES

The mean values and the standard deviations of the positions of the cubes, based on 20 experiments with "positive size-gradient arrangements," are listed in Table B.1. The mean values and the standard deviations of the positions of the cubes, based on 40 experiments with "positive size-gradient arrangements," are listed in Table B.2.

TABLE B.1 Mean value and standard deviation of the positions of the cubes, based on 20 positive size-gradient simulations.

Position [cm]	Mean value				Standard deviation			
	20 mm	16 mm	12 mm	8 mm	20 mm	16 mm	12 mm	8 mm
3	0.850	2.600	9.950	51.650	1.182	2.542	5.042	12.914
4	0.150	0.200	0.900	4.750	0.366	0.523	1.165	3.385
5	0.300	0.550	0.650	3.550	0.571	0.759	0.587	3.236
6	0.500	0.750	1.000	2.500	0.827	0.716	1.376	2.188
7	0.250	0.400	1.000	1.600	0.550	0.598	1.076	1.429
8	0.250	0.650	1.250	1.350	0.444	0.875	1.020	2.661
9	0.350	0.600	1.100	0.900	0.489	0.821	1.021	1.334
10	0.200	0.550	0.700	0.550	0.523	0.759	0.733	0.887
11	0.150	0.350	0.700	0.400	0.366	0.671	0.923	0.681
12	0.250	0.200	0.500	0.200	0.444	0.410	0.607	0.410
13	0.050	0.100	0.400	0.200	0.224	0.308	0.598	0.410
14	0.150	0.200	0.450	0.100	0.366	0.410	0.759	0.308
15	0.150	0.300	0.250	0.100	0.366	0.733	0.550	0.308
16	0.100	0.150	0.300	0.000	0.308	0.366	0.470	0.000
17	0.100	0.050	0.300	0.000	0.308	0.224	0.470	0.000
18	0.000	0.000	0.100	0.000	0.000	0.000	0.308	0.000
19	0.050	0.000	0.050	0.000	0.224	0.000	0.224	0.000
20	0.000	0.050	0.050	0.100	0.000	0.224	0.224	0.308
21	0.150	0.300	0.350	0.050	0.366	0.571	0.587	0.224

10969853, 2024, 6, Downloaded from https://onlinelibrary.wiley.com/doi/10.1002/nag.3695 by Readcube (Labtiva Inc.), Wiley Online Library on [07/11/2024]. See the Terms and Conditions (https://onlinelibrary.wiley.com/terms-and-conditions) on Wiley Online Library for rules of use; OA articles are governed by the applicable Creative Commons License

TABLE B.2 Mean value and standard deviation of the positions of the cubes, based on 40 positive size-gradient experiments.

Position [cm]	Mean value				Standard deviation			
	20 mm	16 mm	12 mm	8 mm	20 mm	16 mm	12 mm	8 mm
3	1.050	2.125	8.550	49.725	1.197	2.139	5.514	10.713
4	0.025	0.050	0.325	4.225	0.158	0.221	0.656	3.034
5	0.125	0.300	1.075	3.300	0.335	0.464	0.971	2.053
6	0.550	0.550	1.100	2.050	0.749	0.639	1.081	2.136
7	0.275	0.725	1.475	1.575	0.599	0.751	1.261	1.259
8	0.625	0.750	1.325	1.750	0.628	0.670	1.328	1.822
9	0.325	0.750	1.550	1.350	0.526	0.981	1.300	1.252
10	0.250	0.825	0.975	1.150	0.494	0.874	1.000	1.369
11	0.225	0.525	1.225	0.825	0.423	0.784	1.025	1.010
12	0.225	0.325	0.450	0.675	0.480	0.474	0.597	0.971
13	0.075	0.325	0.600	0.375	0.267	0.572	0.900	0.628
14	0.075	0.175	0.275	0.250	0.267	0.385	0.640	0.588
15	0.050	0.125	0.275	0.175	0.221	0.335	0.506	0.385
16	0.025	0.075	0.350	0.100	0.158	0.267	0.864	0.496
17	0.000	0.150	0.150	0.100	0.000	0.362	0.362	0.304
18	0.025	0.075	0.075	0.075	0.158	0.267	0.267	0.350
19	0.000	0.050	0.125	0.075	0.000	0.221	0.335	0.267
20	0.025	0.000	0.000	0.050	0.158	0.000	0.000	0.221
21	0.050	0.100	0.100	0.175	0.221	0.304	0.304	0.447

10969853, 2024, 6, Downloaded from https://onlinelibrary.wiley.com/doi/10.1002/nag.3695 by Readcube (Labtiva Inc.), Wiley Online Library on [07/11/2024]. See the Terms and Conditions (https://onlinelibrary.wiley.com/terms-and-conditions) on Wiley Online Library for rules of use; OA articles are governed by the applicable Creative Commons License

APPENDIX C: DATA FOR RANDOM CASES

The mean values and the standard deviations of the positions of the cubes, based on 20 experiments with "random arrangements," are listed in Table C.1. The mean values and the standard deviations of the positions of the cubes, based on 40 experiments with "random arrangements," are listed in Table C.2.

TABLE C.1 Mean value and standard deviation of the positions of the cubes, based on 20 random simulations.

Position [cm]	Mean value				Standard deviation			
	20 mm	16 mm	12 mm	8 mm	20 mm	16 mm	12 mm	8 mm
3	1.350	2.200	4.450	12.050	0.671	1.105	2.212	4.763
4	0.550	0.500	1.900	7.000	0.887	0.607	1.447	2.847
5	0.650	0.900	1.350	5.750	0.587	0.852	1.137	3.596
6	0.450	1.100	1.800	5.900	0.686	0.852	1.322	2.989
7	0.300	1.200	1.750	6.300	0.470	1.240	1.251	2.536
8	0.200	0.700	2.100	6.000	0.410	0.979	1.447	2.200
9	0.150	0.700	2.150	6.200	0.366	0.801	1.309	2.285
10	0.050	0.250	1.250	4.650	0.224	0.444	0.910	3.216
11	0.150	0.250	0.750	3.750	0.366	0.444	1.020	2.936
12	0.000	0.050	0.650	2.100	0.000	0.224	0.813	1.586
13	0.100	0.050	0.300	1.750	0.308	0.224	0.571	1.333
14	0.000	0.000	0.250	1.300	0.000	0.000	0.550	0.923
15	0.000	0.000	0.200	0.950	0.000	0.000	0.523	0.945
16	0.000	0.000	0.250	0.700	0.000	0.000	0.444	0.733
17	0.000	0.000	0.250	0.650	0.000	0.000	0.550	0.875
18	0.050	0.000	0.000	0.450	0.224	0.000	0.000	0.686
19	0.000	0.050	0.050	0.350	0.000	0.224	0.224	0.489
20	0.000	0.050	0.150	0.350	0.000	0.224	0.366	0.587
21	0.000	0.000	0.400	1.800	0.000	0.000	0.681	1.989

10969853, 2024, 6, Downloaded from https://onlinelibrary.wiley.com/doi/10.1002/nag.3695 by Readcube (Labtiva Inc.), Wiley Online Library on [07/11/2024]. See the Terms and Conditions (https://onlinelibrary.wiley.com/terms-and-conditions) on Wiley Online Library for rules of use; OA articles are governed by the applicable Creative Commons License

TABLE C.2 Mean value and standard deviation of the positions of the cubes, based on 40 random experiments.

Position [cm]	Mean value				Standard deviation			
	20 mm	16 mm	12 mm	8 mm	20 mm	16 mm	12 mm	8 mm
3	1.500	2.750	5.175	14.050	0.847	1.428	2.406	4.825
4	0.300	0.450	1.025	4.500	0.464	0.552	1.097	2.088
5	0.125	0.525	1.150	5.000	0.404	0.679	0.893	2.184
6	0.275	0.600	1.725	4.000	0.452	0.810	1.281	1.908
7	0.600	0.725	2.050	4.925	0.709	0.679	1.358	2.358
8	0.500	0.975	1.850	5.450	0.641	0.862	1.252	2.037
9	0.350	0.650	1.775	4.900	0.533	0.662	1.074	1.972
10	0.075	0.500	1.875	4.925	0.267	0.506	1.114	1.873
11	0.050	0.400	0.950	4.100	0.221	0.545	1.037	2.073
12	0.175	0.150	0.500	3.825	0.385	0.362	0.784	1.866
13	0.000	0.050	0.550	3.150	0.000	0.221	0.677	1.642
14	0.000	0.050	0.400	2.000	0.000	0.221	0.591	1.240
15	0.000	0.075	0.200	1.575	0.000	0.267	0.464	1.375
16	0.000	0.025	0.200	1.300	0.000	0.158	0.405	0.992
17	0.025	0.025	0.225	0.975	0.158	0.158	0.480	1.000
18	0.000	0.050	0.175	0.650	0.000	0.221	0.385	0.802
19	0.000	0.000	0.050	0.650	0.000	0.000	0.221	0.975
20	0.000	0.000	0.050	0.475	0.000	0.000	0.221	0.751
21	0.025	0.000	0.075	1.550	0.158	0.000	0.267	1.568

10969853, 2024, 6, Downloaded from https://onlinelibrary.wiley.com/doi/10.1002/nag.3695 by Readcube (Labtiva Inc.), Wiley Online Library on [07/11/2024]. See the Terms and Conditions (https://onlinelibrary.wiley.com/terms-and-conditions) on Wiley Online Library for rules of use; OA articles are governed by the applicable Creative Commons License